The Roles of an Expanding Wind Field and Inertial Stability in Tropical Cyclone Secondary Eyewall Formation

CHRISTOPHER M. ROZOFF

Cooperative Institute for Meteorological Satellite Studies, and University of Wisconsin—Madison, Madison, Wisconsin

DAVID S. NOLAN

Rosenstiel School of Marine and Atmospheric Science, University of Miami, Miami, Florida

JAMES P. KOSSIN

National Climatic Data Center, Asheville, North Carolina, and Cooperative Institute for Meteorological Satellite Studies, Madison, Wisconsin

FUQING ZHANG

Department of Meteorology, The Pennsylvania State University, University Park, Pennsylvania

JUAN FANG

Key Laboratory of Mesoscale Severe Weather (MOE), Department of Atmospheric Sciences, Nanjing University, Nanjing, China

(Manuscript received 27 November 2011, in final form 29 March 2012)

ABSTRACT

The Weather and Research and Forecasting Model (WRF) is used to simulate secondary eyewall formation (SEF) in a tropical cyclone (TC) on the β plane. The simulated SEF process is accompanied by an outward expansion of kinetic energy and the TC warm core. An absolute angular momentum budget demonstrates that this outward expansion is predominantly a symmetric response to the azimuthal-mean and wavenumber-1 components of the transverse circulation. As the kinetic energy expands outward, the kinetic energy efficiency in which latent heating can be retained as local kinetic energy increases near the developing outer eyewall.

The kinetic energy efficiency associated with SEF is examined further using a symmetric linearized, nonhydrostatic vortex model that is configured as a balanced vortex model. Given the symmetric tangential wind and temperature structure from WRF, which is close to a state of thermal wind balance above the boundary layer, the idealized model provides the transverse circulation associated with the symmetric latent heating and friction prescribed from WRF. In a number of ways, this vortex response matches the azimuthal-mean secondary circulation in WRF. These calculations suggest that sustained azimuthal-mean latent heating outside of the primary eyewall will eventually lead to SEF. Sensitivity experiments with the balanced vortex model show that, for a fixed amount of heating, SEF is facilitated by a broadening TC wind field.

1. Introduction

Secondary eyewall formation (SEF) in tropical cyclone (TC) eyewall replacement cycles (ERCs) (e.g., Willoughby et al. 1982; Sitkowski et al. 2011, 2012) has sustained attention in the TC community for decades because of its elusive predictability and significant impact on TC structure and intensity change. Beyond the sensitivity of numerical TC simulations to convective-scale processes, part of the challenge in operational forecasting is that the exact physical factors responsible for SEF have not been discerned from a list of plausible mechanisms. In recent years, improved resolution in full-physics TC simulations has resulted in numerous studies of SEF and ERCs (e.g., Zhang et al. 2005; Terwey

Corresponding author address: Christopher Rozoff, Cooperative Institute for Meteorological Satellite Studies, University of Wisconsin—Madison, 1225 West Dayton Street, Madison, WI 53706. E-mail: chris.rozoff@ssec.wisc.edu

DOI: 10.1175/JAS-D-11-0326.1

and Montgomery 2008; Wang 2008a,b, 2009; Hill and Lackmann 2009; Hogsett and Zhang 2009; Wu et al. 2009; Judt and Chen 2010; Martinez et al. 2011; Zhou and Wang 2011; Abarca and Corbosiero 2011; Chen et al. 2011; Wu et al. 2012; Huang et al. 2012, hereafter HMW12; Fang and Zhang 2012, hereafter FZ12). This suggests that the understanding and predictability of SEF will continue to improve.

Early theory on SEF that is still relevant today focused on idealized, axisymmetric models in thermal wind balance. Generally, the idea was to understand the TC system-scale response to adding a heat source outside of the radius of maximum wind (RMW) of a TC-like vortex. Using a variation of the Eliassen (1951) transverse circulation equation for axisymmetric, balanced flow, Shapiro and Willoughby (1982, hereafter SW82) studied the impacts of adding point sources of diabatic heating to the region outside of the RMW for a variety of tangential wind profiles. They specifically found that when the tangential wind decays more slowly with radius, the enhanced inertial stability reduces the low-level radial inflow. However, the larger angular momentum associated with the broader wind field more than compensates for the reduced inflow and thereby increases the tangential wind tendency near the heat source. Using a similar model, Schubert and Hack (1982, hereafter SH82) and Hack and Schubert (1986, hereafter HS86) elucidated the existence of a nonlinear instability in which diabatic heating can increasingly induce larger tangential wind tendencies as inertial stability increases in the region of heating.

More recent literature has established the importance of asymmetric perturbations in vortex evolution. One of the simplest models used in studying the dynamics of vortex asymmetries and their role in SEF is the two-dimensional (2D) nondivergent barotropic model. In the unforced, barotropic framework, Kuo et al. (2004, 2008) proposed that concentric vorticity rings can evolve from certain initial conditions consisting of one or more patches of weaker vorticity in the vicinity of a strong TC-like vortex. However, Moon et al. (2010) showed that small-scale, high-amplitude vorticity perturbations arising from processes such as rainband convection are more typical outside of the eyewall of a mature TC and that these perturbations do not axisymmetrize into concentric vorticity rings.

The barotropic framework has also been used to develop theory for vortex Rossby waves (VRWs) and their connections to vortex axisymmetrization (e.g., Guinn and Schubert 1993; Montgomery and Kallenbach 1997). Montgomery and Kallenbach hypothesized that VRW interactions with the mean flow may contribute to SEF. In particular, a negative radial vorticity gradient of finite width outside of the RMW supports the outward propagation of VRWs until the waves slow down toward the stagnation radius where the VRW group velocity goes to zero. Inside this stagnation radius, cyclonic eddy momentum is transported inward and may contribute to SEF in this region. In this same framework, Martinez et al. (2010) analyzed the nonlinear evolution of asymmetric vorticity perturbations produced by barotropic instability in the symmetric mean vortex. Their analysis diagnosed wave–mean flow interactions that produced a secondary wind maximum near the critical radius of leading modes in their numerical experiment. The neglect of the three-dimensional (3D) dynamics, friction in the boundary layer, and convective processes is a serious limitation of any barotropic study. Overall, the role of axisymmetrization in SEF requires further examination in 3D modeling frameworks.

Given the 3D nature of SEF, Terwey and Montgomery (2008) proposed a β-skirt axisymmetrization (BSA) mechanism incorporating both barotropic dynamics and 3D convective processes. In this mechanism, SEF is initiated by the anisotropic upscale cascade of convectively generated potential vorticity (PV) anomalies on a low-level, negative PV gradient (i.e., β skirt) outside of the RMW. The collocation of convection and the β skirt are necessary conditions for SEF in this hypothesis. Qiu et al. (2010) find that SEF occurs near the VRW stagnation radius and in a convectively active region of their simulated TC's β skirt. They further revealed that the eddy momentum flux convergence near the stagnation radius led to the outward expansion of the β skirt. The full-physics TC simulations of Hogsett and Zhang (2009), Martinez et al. (2011), and Abarca and Corbosiero (2011) also emphasize the potential role for VRWs in SEF.

Regardless of the mechanisms that may spin up the wind field and/or force latent heating outside of the primary eyewall, a number of studies stress the importance of dynamical adjustment to latent heating in SEF and size evolution. Using an idealized model, Moon and Nolan (2010) showed that realistic distributions of asymmetric diabatic heating from stratiform and convective precipitation in outer rainbands can induce secondary wind maxima and other circulation features often observed in rainbands. Some studies (Wu et al. 2009; Judt and Chen 2010) have carried out PV budgets in TC simulations to show that the PV generation from concentrated rainband activity in the incipient outer eyewall region is key to SEF. Wang (2009) found that artificially increasing latent heating in the region of outer rainbands of simulated TCs led to SEF and an outward expansion of winds. Hill and Lackmann (2009) showed that enhancing the environmental relative humidity facilitates

SEF and larger simulated TCs. This latter result is consistent with idealized balance model results described in Nong and Emanuel (2003), who showed that, along with wind-induced surface heat exchange (WISHE) and finite-amplitude perturbations, relative humidity may be an important factor in SEF. The importance of relative humidity in SEF has been supported by the observational study of Kossin and Sitkowski (2009). Similarly, a series of papers by Xu and Wang (2010a,b) suggests that the distribution of low-level moist entropy and initial vortex size impact the size of a TC. Finally, an idealized full-physics TC simulation by FZ12 on the β plane showed that β shear in a motionless environment can impose a significant heating asymmetry that promotes the generation of an outer eyewall. This β shear results from the height variation of the TC circulation's advection of planetary vorticity (Ritchie and Frank 2007).

Along with the developing body of work on dynamical adjustment, recent work suggests that unbalanced processes are relevant to SEF as well. HMW12 used the full-physics TC simulation of Wu et al. (2012) to understand symmetric aspects of SEF. Consistent with the studies of Smith et al. (2008, 2009) and Smith and Montgomery (2010), HMW12 suggest that an expanding wind field in and above the boundary layer leads to increased boundary layer inflow due to an inward pressure gradient force that exceeds the counteracting but frictionally reduced centrifugal force. Because of the net increase in absolute angular momentum in a region of strong inflow, supergradient winds can develop in and just above the boundary layer. An adverse pressure gradient force associated with the supergradient winds may enhance low-level convergence and facilitate SEF. Using airborne Doppler radar and dropsonde data from Hurricane Rita (2005), Didlake and Houze (2011) found supergradient forces exist in the boundary layer near Rita's outer eyewall.

Taken together, the above studies suggest that SEF is likely a dynamical adjustment process to heating that may be augmented by unbalanced processes in the boundary layer. From this point of view, a more complete theory for SEF requires fully resolving where, when, and how quickly rainband activity will transform into an outer eyewall. With evidence that a broader vortex structure increases the local production of kinetic energy in a region of enhanced latent heating (e.g., SW82; HS86; Xu and Wang 2010b), we propose that the vortex inertial stability structure helps control the likelihood and speed of SEF as well. Using data from a realistic simulation of a TC, we now have the ability to evaluate pioneering theoretical predictions (e.g., SW82) with realistic time-evolving fields of vortex structure and diabatic and frictional forcing. Here, we use a high-resolution numerical simulation of SEF in a TC to examine the TC response to diabatic heating and frictional forcing and the role of the TC's response in SEF and structure change. Section 2 briefly describes the full-physics model setup. Basic aspects of the TC simulation and the SEF event in the simulation are described in section 3. Section 4 describes processes governing TC structure change and their impact on kinetic energy efficiency. Section 5 examines the role of inertial stability in SEF from the perspective of a balanced vortex model. Finally, discussion and conclusions are provided in section 6.

2. Model setup

This study utilizes the Advanced Research Weather Research and Forecast Model (WRF) version 2.2 (Skamarock et al. 2005) to simulate an intense TC in an idealized setting. The simulation is carried out on the β plane with three domains containing horizontal grid spacing of 9, 3, and 1 km and domain sizes of $10\,800 \times 10\,800$ km^2, 1620×1620 km^2, and 1000×1000 km^2, respectively. Two-way interactive nesting is used with vortex-following nested domains. As a result, the model TC is always situated in the center of the finest domain. The model has 35 vertical levels with the model top near 28 km. The vertical grid spacing is stretched from 0.6-km spacing near the surface to 3.6-km spacing near the top of the model domain. Radiation is neglected as in Nolan (2007) to suppress convection on the outer grids. The WRF Single-Moment (WSM) six-class scheme with graupel (Hong et al. 2004) is used. This simulation contains no large-scale environmental flow and the outer spiral rainbands are nearly contained within the finest domain. As such, cumulus parameterization is not included in any grid. Turbulent fluxes are parameterized using the Yonsei University (YSU) planetary boundary layer scheme (Noh et al. 2003).

The simulation is initialized with an axisymmetric cyclonic vortex similar to that used by Rotunno and Emanuel (1987) in a quiescent atmosphere and over the ocean with a constant sea surface temperature of 29.15°C. The initial unperturbed atmospheric temperatures are obtained from the Jordan (1958) mean hurricane season sounding for the Caribbean. The initial baroclinic vortex is centered at 20°N and in gradient-wind balance with the maximum azimuthal wind speed of 16 m s^{-1} at a radius of about 102 km, equivalent to a strong tropical depression.

3. Simulation overview

The TC simulation studied here is similar to the lower resolution (3-km horizontal grid spacing) simulation

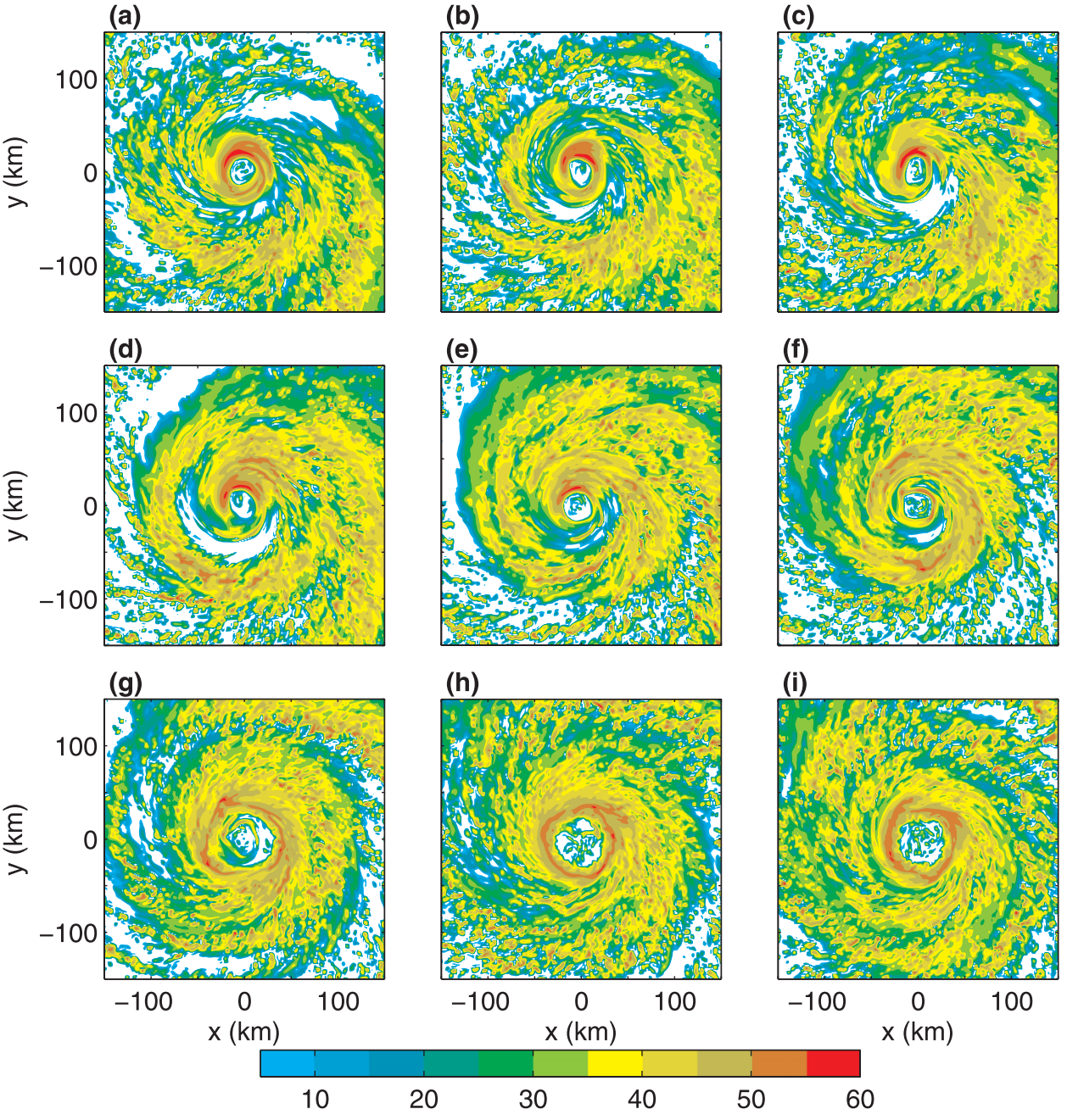

FIG. 1. Low-level (z = 1 km) synthetic radar reflectivity (dBZ) at (a) 102, (b) 107, (c) 112, (d) 117, (e) 122, (f) 127, (g) 132, (h) 137, and (i) 142 h.

examined in FZ12. In FZ12, a wavenumber-1 pattern of stratiform rainband precipitation resulting from β shear led to evaporative cooling and a subsequent sharpening of the low-level equivalent potential temperature θ_e gradient outside the primary eyewall. This gradient coincided with a region of convective initiation preceding SEF. The SEF event analyzed in the current simulation also emerged as the β shear weakened and the rainband activity symmetrized. We focus on a time frame corresponding to SEF that covers the 72–144-h period of simulation. A brief overview of the general evolution during this time frame is now presented.

The low-level (z = 1 km) synthetic radar reflectivity in Fig. 1 provides an overview of the precipitation during the simulated ERC. During the 102–127-h time frame, asymmetric rainband activity 50–100 km from the center

organizes into a more symmetric outer eyewall. Also, moat formation appears early. At 102 h (Fig. 1a), a weak radar echo region materializes on the southern and eastern sides of the eyewall while more vigorous rainbands are found farther out from center. Pronounced clearing around the outer edge of the eyewall was evident even earlier than 102 h (not shown). In the next 25 h (Figs. 1b–f), a wavenumber-1 asymmetry persists in the moat, with weaker radar echoes appearing on the southern side of the primary eyewall. Beyond the region of SEF, there is a broad wavenumber-1 pattern of concentrated rainfall that rotates from south to north during this period. By 127 h (Fig. 1g), a concentric eyewall configuration exists. Eyewall replacement follows over the next 10 h and results in a larger eye (Figs. 1h,i).

Hovmöller diagrams highlight basic kinematic and thermodynamic changes throughout the period preceding and accompanying the ERC. Figure 2a shows the low-level (z = 1 km) azimuthal-mean synthetic radar reflectivity. A moat of low precipitation clearly emerges in the azimuthal-mean state before SEF occurs. This low-precipitation moat moves inward with time. At about 95 h, the intensity of radar reflectivity in the eyewall increases as an earlier, minor ERC-like process completes. The outer eyewall precipitation starts out diffuse between 60- and 140-km radius (95–115 h), but it eventually solidifies into a more coherent structure (115–125 h). Consistent with most ERCs, the outer eyewall contracts inward with time.

The midlevel (z = 5 km) azimuthal-mean vertical wind (Fig. 2b) progresses similarly to the radar reflectivity. Weak subsidence begins to appear outside of the primary eyewall around 95 h as the primary eyewall intensifies. Not until the outer eyewall becomes more symmetric does the Hovmöller diagram indicate substantial upward motion outside of the moat (~125 h). The radial structure of tangential wind evolves rapidly during this time as well. Figure 2c shows the tangential wind at z = 0.5 km. Even before the ERC takes place, the tangential wind generally expands outward with time. However, there is a local weakening and contraction of tangential winds just outside the RMW after the earlier ERC-like process completes around 95 h. A sharp and rapid expansion of the tangential winds occurs after 105 h in association with SEF. A striking secondary tangential wind maximum in the azimuthal mean is never indicated near the time of SEF. Individual cross sections, however, indicate that clear secondary wind maxima appear in just some sectors of the TC (e.g., Fig. 3). Also, consistent with the flight-level data studied in Sitkowski et al. (2011), these secondary wind maxima are evident before concentric eyewalls have clearly emerged in the precipitation fields.

Figure 2d shows the low-level radial flow evolution during an ERC. Some weak outward flow is seen in the eye throughout the entire time period, whereas the flow is generally inward outside of the primary eyewall. Low-level inflow increases significantly as the primary eyewall's convection intensifies at 95 h, but thereafter it progressively weakens as the moat and outer eyewall develop. Stronger inflow develops outside of the outer eyewall by 125 h. It is worth noting that outside of 80–100 km, the low-level inflow intensifies well before SEF.

Azimuthal-mean low-level (z = 0.5 km) temperature and θ_e fields are provided in Figs. 2e and 2f. Between 75 and 100 h, air cooler than 22°C exists in the region of precipitation shown in Fig. 2a due to cool downdrafts. As the moat matures, warmer temperatures emerge in this region, likely tied to subsidence warming, downward mixing into the boundary layer, and the relatively warm sea surface temperatures below. This pattern is also noticeable in the θ_e field as well. However, in response to the expanding low-level wind field and increased latent heat flux at the ocean surface, the θ_e field still generally expands outward. The rapid outward increase in θ_e at around 100 h is similar to an increase seen in FZ12. Moreover, the radial gradient of θ_e sharpens around 60–100 km from center at this time. As indicated in Fig. 2a, this region experiences invigorated precipitation at this time. In comparison to FZ12, the spatial scales of the inner and outer eyewalls are smaller in this higher-resolution simulation, but otherwise both simulations are similar. As discussed in FZ12, this frontlike structure may expedite SEF.

4. Symmetric aspects of secondary eyewall formation

a. Absolute angular momentum budget

To assess symmetric aspects of SEF, we now focus our attention more closely on the 48-h period following 96 h, which captures SEF and the subsequent ERC. A rapid expansion of tangential winds occurs during this time frame. An absolute angular momentum budget is carried out to illustrate the leading contributions to the expansion of the winds.

An absolute angular momentum budget in cylindrical coordinates centered over the center of the simulated TC can be directly obtained from the equation for tangential wind. The tangential wind equation is

$$\frac{\partial v}{\partial t} + u\frac{\partial v}{\partial r} + v\frac{\partial v}{r\partial \lambda} + w\frac{\partial v}{\partial z} + u\left(f + \frac{v}{r}\right) = -\frac{1}{r\rho}\frac{\partial v}{\partial \lambda} + F_{\lambda}, \tag{1}$$

where u, v, and w are the radial, tangential, and vertical components of the wind; r, λ, and z are the radial,

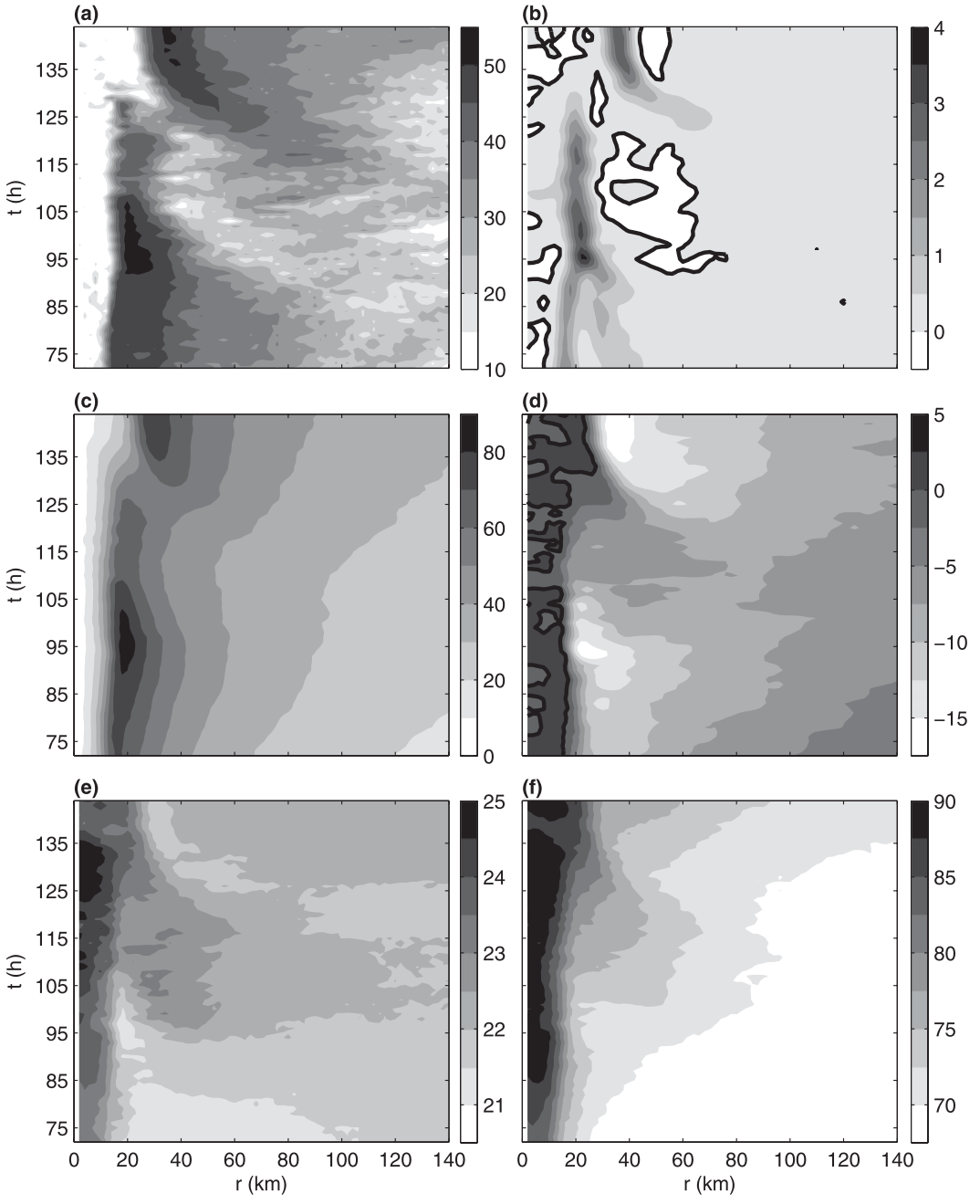

FIG. 2. Hovmöller diagrams of the azimuthal-mean (a) synthetic radar reflectivity (dBZ) at $z = 1$ km, (b) vertical velocity (m s^{-1}; the zero contour is thick black) at $z = 5$ km, (c) tangential wind (m s^{-1}) at $z = 0.5$ km, (d) radial wind (m s^{-1}; the zero contour is in thick black) at $z = 0.5$ km, (e) temperature (°C) at $z = 0.5$ km, and (f) equivalent potential temperature (°C) at $z = 0.5$ km.

tangential, and physical height coordinates; and t, f, ρ, p, and F_λ are time, the Coriolis parameter (where $f = f_o + \beta y$), density, pressure, and tangential component of friction/diffusion, respectively. By multiplying (1) by r, noting the definition of absolute angular momentum is $M = (1/2)fr^2 + rv$, breaking variables into azimuthal mean and perturbation quantities (i.e., $\psi = \overline{\psi} + \psi'$ for any variable ψ), and taking the azimuthal average of all terms, noting that $\overline{\zeta_a} = \overline{f} + \partial(r\overline{v})/r\partial r$ is the azimuthal mean vertical component of absolute vorticity, and after some manipulation of terms, we can obtain an equation for the local time rate of change of azimuthal mean M:

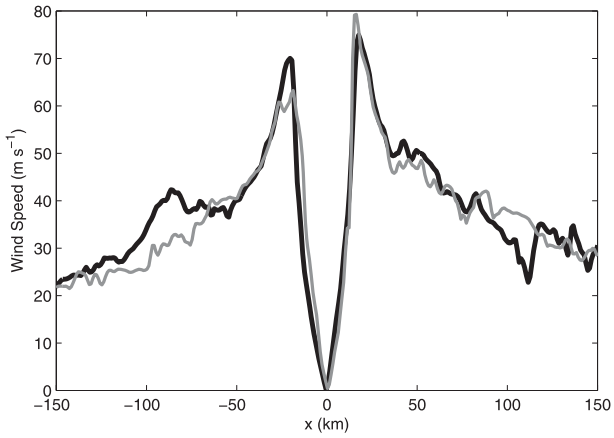

FIG. 3. South-to-north cross section of the zonal wind (gray) and west-to-east cross section of the meridional wind (black) at z = 0.5 km and 122 h.

$$\frac{\partial \overline{M}}{\partial t} = -r\overline{u}\overline{\zeta_a} - \overline{w}\frac{\partial \overline{M}}{\partial z} - r\overline{u'\zeta_a{}'} - \overline{w'\frac{\partial M'}{\partial z}} - \overline{\frac{1}{\rho'}\frac{\partial p'}{\partial \lambda}} + r\overline{F_\lambda}. \tag{2}$$

On the right-hand side of (2), the first and third terms together represent the total radial flux of absolute vorticity, the second and fourth terms are the vertical advection of M, the fifth term is the eddy pressure gradient term (negligible compared to the other terms), and the final term provides the impact of friction and diffusion.[1] To perform a budget, variables from WRF are interpolated to cylindrical coordinates centered on the centroid of vertical vorticity ζ. Thereafter, all terms are computed in (2) at 6-min intervals in order to numerically integrate (2) forward in time. Actual changes in $\overline{M}$ over 1-h time periods are compared to estimated changes based on the right-hand side of (2) in order to determine whether the budget reliably captures processes that affect $\overline{M}$. Hour-long time periods are chosen since the rapid eyewall contraction washes out coherent signals over larger integration intervals.

Figure 4 shows an example of the $\overline{M}$ budget for 114–115 h. It is quite typical of other hour-long periods during SEF but it is also a critical time in the SEF process marking the stage when the secondary eyewall is becoming noticeable in many symmetric fields. During this time, a rapid expansion in the $\overline{v}$ field is occurring (cf. Fig. 2). As seen in Fig. 4a, $\overline{M}$ is increasing by levels exceeding 1×10^5 m^2 s^{-1} h^{-1} throughout the troposphere over r = 80–150 km. This also is a region of positive latent heating. Figure 4b is provided to evaluate how well the sum of individual $\overline{M}$ -budget terms reproduces the actual change in $\overline{M}$. Near the surface, there is little agreement between the estimated and actual changes in $\overline{M}$ and there are even sign errors outside of r = 80 km. Above 1-km height, the qualitative agreement is best outside of r = 80 km, whereas the agreement is more marginal in the inner core. SEF is beginning to appear at this time just outside of r = 80 km. The agreement between the estimated and actual $\overline{M}$ in the region of the outer eyewall is good throughout the ERC. Consistent with previous $\overline{M}$-budget calculations (Xu and Wang 2010b; Qiu et al. 2010), a significant fraction of the low-level $\overline{M}$ expansion is a result of the symmetric low-level inward flux of $\overline{\zeta_a}$ (or alternatively, the symmetric low-level inward advection of $\overline{M}$) (Fig. 4d). [In passing, it is worth noting that budget calculations for $\overline{u}$ show that increasing rapid low-level inflow near the developing outer eyewall is the result of a frictionally weakened low-level $\overline{v}$ that cannot balance the strong low-level radial pressure gradient (not shown)]. The low-level inward flux of $\overline{\zeta_a}$ is countered somewhat by the friction and diffusion term (Fig. 4c). Vertical advection of $\overline{M}$ enhances $\overline{M}$ throughout the depth of the troposphere in the vicinity of the concentrated latent heating (Fig. 4e). Overall, as seen in Fig. 4f, the symmetric mean circulation contributes substantially to the $\overline{M}$ budget. However, there is a nontrivial contribution to the enhancement of $\overline{M}$ in the region of SEF by the asymmetric components of the $\overline{M}$ budget (Figs. 4g–i). These contributions are predominantly from wavenumber-1 azimuthal perturbations that correspond spatially with the wavenumber-1 structure in latent heating (not shown). Overall, the spinup of the outer eyewall results from the secondary circulation, which is tied to both Ekman pumping and latent heating. As discussed earlier, the importance of diabatic heating in spinning up an outer eyewall or expanding the wind field has been emphasized in earlier research.

b. *On the kinetic energy efficiency of secondary eyewall formation*

In assessing the role of balanced vortex dynamics in SEF, an insightful way to describe the azimuthal-mean kinematic structure is with the inertial stability parameter:

$$I^2 = \left(\overline{f} + \frac{2\overline{v}}{r}\right)(\overline{f} + \overline{\zeta}). \tag{3}$$

Increased I creates resistance to radial flow (e.g., SH82; SW82; HS86). Therefore, it is expected that diabatic heating occurring in a region of enhanced I

[1] It should be noted that (1) and (2) use ground-relative wind speeds. The storm, on average, moves toward the northwest at 1.8 m s^{-1} due to the β effect, but a budget for storm-relative winds produces virtually identical results and is therefore not included.

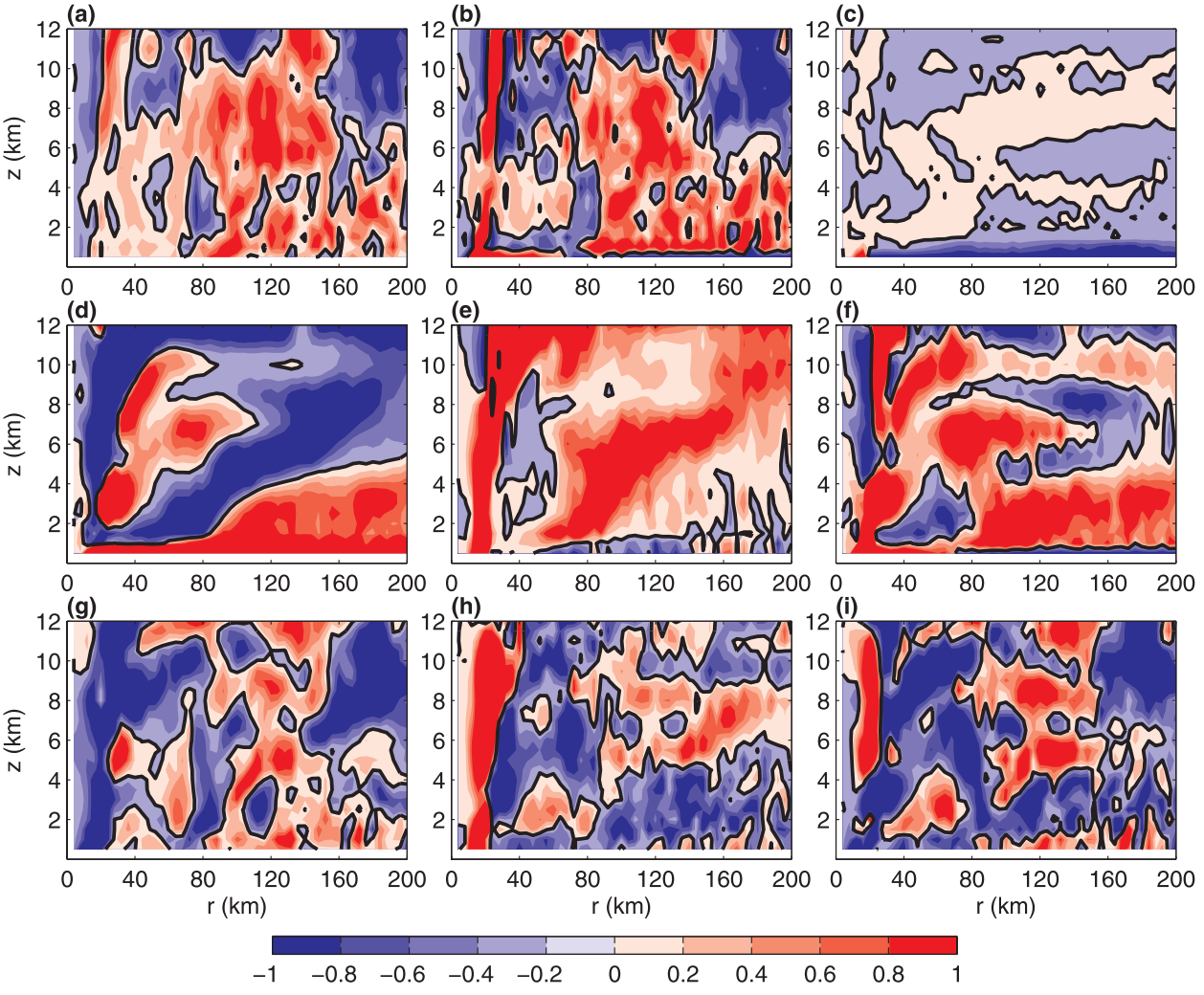

FIG. 4. The (a) actual and (b) diagnosed changes in $\overline{M}$ from 114 to 115 h. Also, the (c) frictional ($r\overline{F_\lambda}$), (d) symmetric radial vorticity flux ($-r\overline{u}\overline{\zeta_a}$), (e) symmetric vertical $\overline{M}$ advection ($-\overline{w}\partial\overline{M}/\partial z$), (f) total symmetric ($-r\overline{u}\overline{\zeta_a} - \overline{w}\partial\overline{M}/\partial z + r\overline{F_\lambda}$), (g) asymmetric radial vorticity flux ($-\overline{ru'\zeta_a'}$), (h) asymmetric vertical advection ($-\overline{w'\partial M'/\partial z}$), and (i) the total asymmetric ($-\overline{ru'\zeta_a'} - \overline{w'\partial M'/\partial z}$) contributions to the change in $\overline{M}$ from 114 to 115 h. Changes in $\overline{M}$ are expressed in units of 10^5 m^2 s^{-1} h^{-1}.

should lead to more confined subsidence and enhanced adiabatic compressional warming. As absolute angular momentum is advected inward and the inertial stability builds up in this region, it is worthwhile to consider the extent to which this increased inertial resistance increases the efficiency with which latent heating can locally warm the troposphere and increase the tangential winds.

Figure 5a provides a snapshot of I at 97 h, which is prior to the SEF event. To emphasize the low-level skirt of I extending outward from the primary eyewall, values of I exceeding 3×10^{-3} s^{-1} are not contoured in the eye–eyewall region. Much larger values of I (exceeding 7×10^{-3} s^{-1}) are found in the vicinity of the primary eyewall, which coincide with the strongest $\overline{v}$ there and a local maximum in $\overline{\zeta}$. Consistent with thermal wind balance and the $\overline{v}$ structure at this time, the azimuthal-mean potential temperature $\overline{\theta}$ shown in Fig. 5b indicates a compact warm-core structure at 97 h.

Over the next 15 h (97–112 h), I increases throughout the troposphere outside of the primary eyewall (Fig. 5c). In the region defined by $40 \le r \le 60$ km and $z \le 5$ km, the average value of I increases by 25% (0.17×10^{-3} s^{-1}). There is also a substantial reduction of I in the core of the TC coinciding with decreased $\overline{v}$ in the primary eyewall. Figure 5d shows the change in $\overline{\theta}$ from 97 to 112 h, which has increased by 1–3 K outside of the primary eyewall. Over the subsequent 15 h (Figs. 5e,f), I and $\overline{\theta}$ change more dramatically than in the first 15 h. The average value of I over the region given by

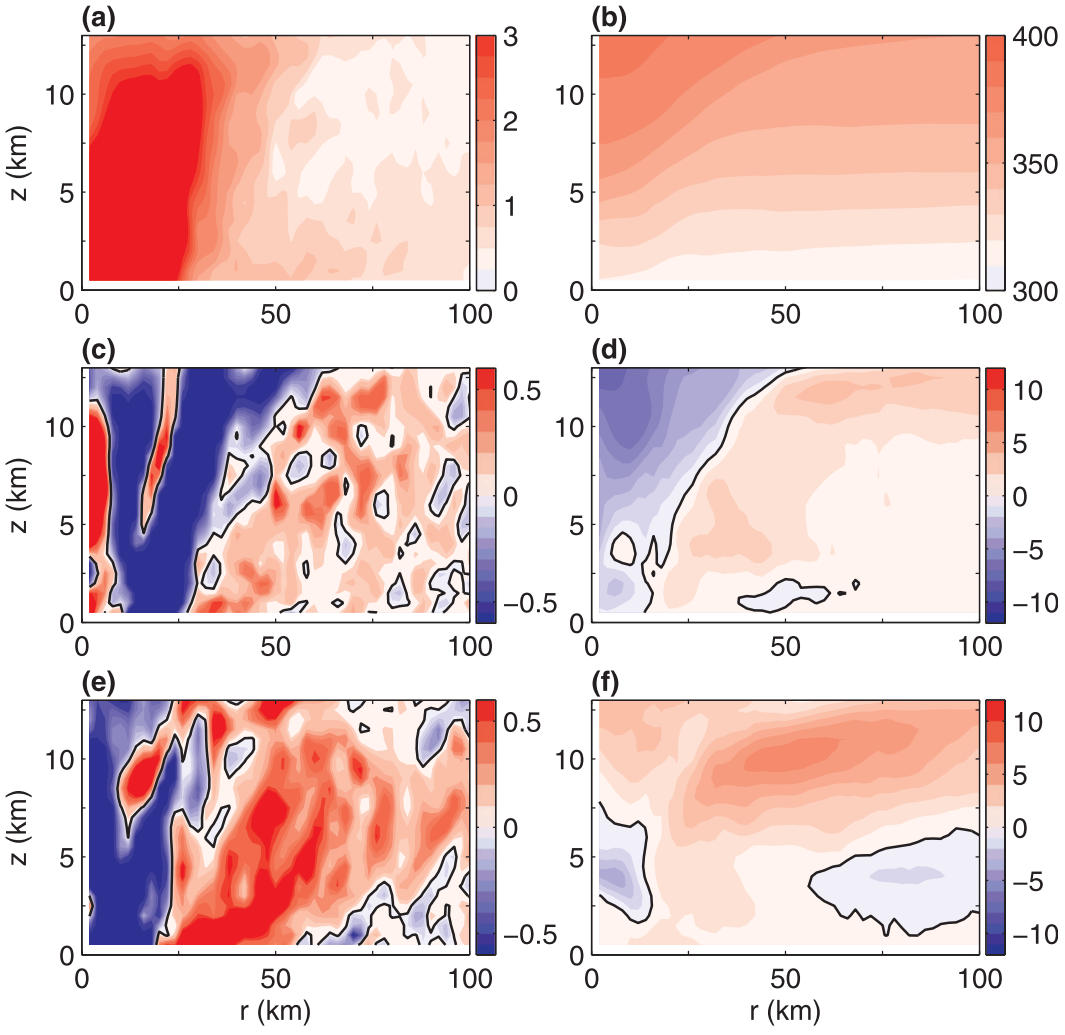

FIG. 5. The parameters (a) I (10^{-3} s^{-1}) and (b) $\overline{\theta}$ (K) at 97 h. The change in (c) I (10^{-3} s^{-1}) and (d) $\overline{\theta}$ (K) between 97 and 112 h. (e),(f) As in (c),(d), but between 112 and 127 h.

$40 \le r \le 60$ km and $z \le 5$ km increases by 56% (0.47×10^{-3} s^{-1}) from 112 to 127 h. Outside of the primary eyewall, $\overline{\theta}$ increases from around 1–4 K in the lower troposphere to 4–10 K in the upper troposphere. In other words, the intensification of the vortex in the moat and developing outer eyewall regions accelerates with time.

Figure 6a shows the midlevel I and the azimuthal-mean vertical wind $\overline{w}$ (which is closely correlated with latent heating) from 72 to 144 h. The radial expansion of I through this time period corresponds with an expanding $\overline{v}$ field (Fig. 2c). There is also a temporary decrease in I in the moat region (~90–110 h) leading up to SEF. After SEF occurs, I increases more rapidly in the vicinity of the developing outer eyewall. As the incipient outer eyewall contracts between 115 and 135 h, its latent heating moves into a region containing higher and intensifying I.

Another way to view the kinematic evolution of SEF is to compute the integrated symmetric kinetic energy (KE), defined here as

$$\mathrm{KE} = 2\pi \int_{r_1}^{r_2} \int_{0}^{z_t} \overline{\rho} \frac{1}{2} (\overline{u}^2 + \overline{v}^2 + \overline{w}^2)\, dz\, r\, dr, \qquad (4)$$

where r_1, r_2, and z_t are the inner radius, outer radius, and upper bound of the region of integration. The results for $r_1 = 0$ km, $r_2 = 200$ km, and $z_t = 13$ km are shown in Fig. 6b. The decrease in $\overline{v}$ prior to SEF is substantial enough to lead to a temporary decrease in KE. Consistent with observations of ERCs (e.g., Maclay et al. 2008; Sitkowski et al. 2011), a substantial increase in KE (about 79%) occurs between 115 and 144 h as the ERC takes place. Figure 6b also shows the integrated symmetric heat q released by microphysical processes:

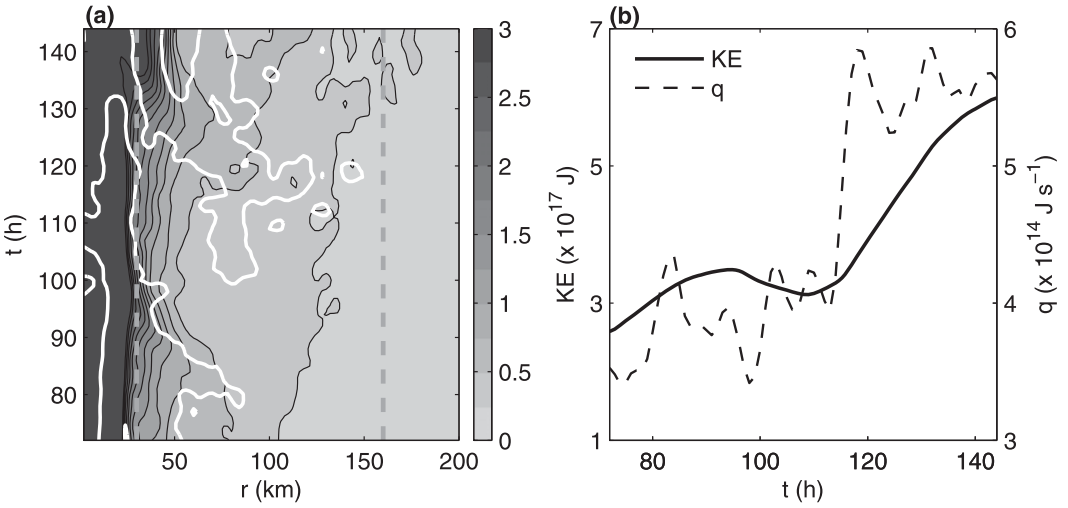

FIG. 6. (a) Hovmöller (radius–time) diagram of I (10^{-3} s^{-1}; shaded) and $\overline{w}$ (white 0.2 m s^{-1} isotach) at $z = 5$ km. (b) KE (10^{17} J; solid) and q (10^{14} J s^{-1}; dashed) as functions of time. The vertical dashed lines in (a) are the radial bounds for the calculations in Fig. 7.

$$q = 2\pi \int_{r_1}^{r_2} \int_{0}^{z_t} \overline{\rho} \frac{c_p \overline{T}\overline{\theta}}{\overline{\theta}} \, dz \, r \, dr, \tag{5}$$

where c_p is the specific heat of dry air at constant pressure, $\overline{\theta}$ is the azimuthal-mean microphysical contribution to latent heating, and $\overline{T}$ is the azimuthal-mean temperature. The temporal evolution of q is noisy but fairly steady except for a jump in heating as SEF begins. A similar increase in precipitation was noted in FZ12 as the β shear abated and the rainband precipitation became more symmetric. After an upward jump, q remains at an elevated state. This jump precedes increasing KE. This time lag is consistent with the absolute angular momentum budget shown in Fig. 4 and with the results of Xu and Wang (2010b), which emphasize the secondary circulation's dominant role in strengthening the outer wind field.

An empirical way to determine the role of efficiency in the simulated SEF process is to estimate the degree to which latent heating associated with convective and stratiform clouds is retained in the TC's inner core as kinetic energy. Similar to Nolan et al. (2007, hereafter NMS07), we define the kinetic energy efficiency (KEE) as the ratio of the change in KE (ΔKE) over a 6-h time period to the time integral of q (Q) over a 6-h period[2] (i.e., KEE = ΔKE/Q). We can compute the KEE for the entire region shown in Fig. 6a, but we instead focus on a fixed region large enough to capture the immediate surroundings of a contracting outer eyewall yet small enough so that the time-varying diabatic heating associated with the inner eyewall does not interfere with interpretation of the results. Specifically, we compute (4) and (5) with $r_1 = 30$ km, $r_2 = 160$ km, and $z_t = 13$ km, as depicted by the vertical dashed lines in Fig. 6a. The area average of I at $z = 5$ km over this radial region is provided in Fig. 7a. There is a noteworthy jump of about 2×10^{-4} s^{-1} in the area-average I from 115 to 130 h corresponding in time with SEF. In this same outer eyewall region, both KE and q (Fig. 7b) evolve in a similar way as these variables over the broader domain (Fig. 6b), where a jump in q precedes the increase in KE. Some of this jump is simply the result of a temporary spike in more widespread latent heating prior to a more coherent outer eyewall structure. Not surprisingly, the area-average I correlates with KE with a Pearson correlation coefficient of 0.959, but the overall volumetric KE lags behind the midlevel I slightly such that I and q evolve more closely with one another ($r = 0.895$) than KE and q ($r = 0.795$). Figure 7c shows the 6-h change in KE and q integrated over the previous 6 h. The 6-h increase in KE jumps from negative values to over 5×10^{16} J between 111 and 121 h, which follows an uptick in the heat injection around 100 h. The KEE is plotted in Fig. 7d. Consistent with the KEE calculations in NMS07, the KEE is generally very small (<0.7%), indicating that much of the heat released never converts into localized KE and/or the KE is hampered by friction. Nonetheless, the KEE increases rapidly from 0.3% to 0.6% during SEF (115–120 h). Overall, the instantaneous inertial stability does provide a rough sense of kinetic energy

[2] Experimentation of time intervals between 1 and 6 h for the time integration of q and for ΔKE and time lags of 1–6 h between Q and ΔKE yielded similar results.

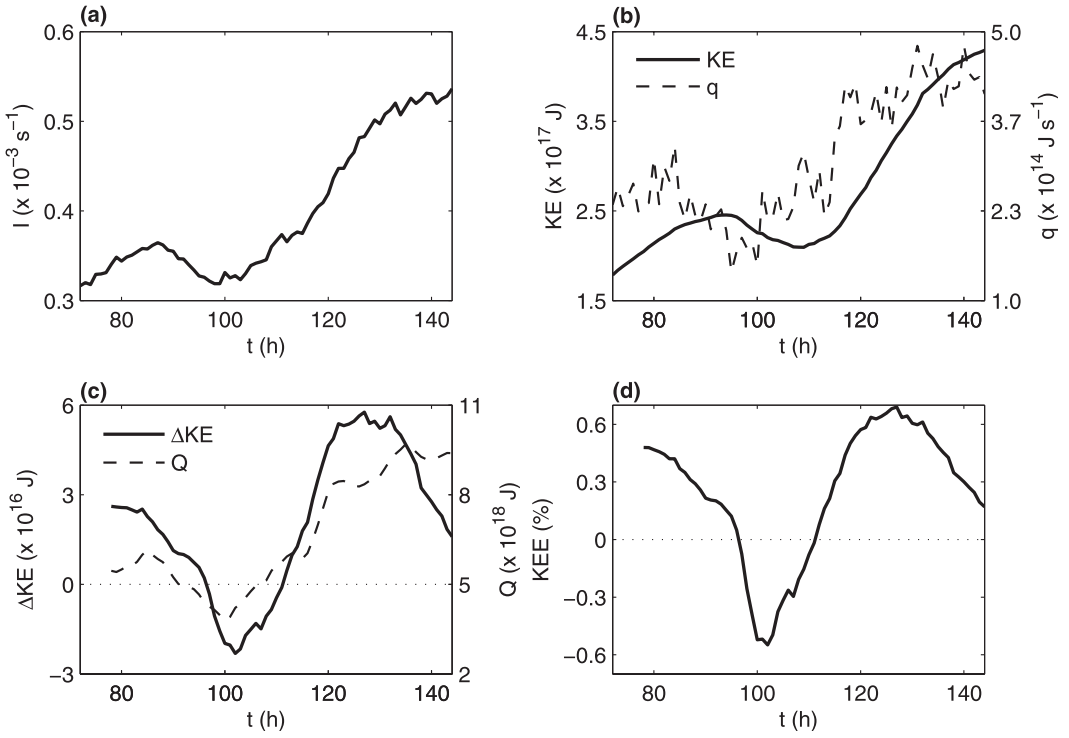

FIG. 7. (a) The area average of I at $z = 5$ km (10^{-3} s^{-1}), (b) KE (10^{17} J; solid) and q (10^{14} J s^{-1}; dashed), (c) ΔKE (10^{16} J; solid) and Q (10^{18} J; dashed), and (d) KEE (%) for the radial region bounded by the vertical dashed lines in Fig. 6a.

efficiency, but it is more meaningful to directly compare the change in KE following a period of heating. The role of KEE in SEF will be examined more closely in the next section.

5. Balanced aspects of secondary eyewall formation

a. Diagnosis of balanced aspects of SEF with WRF data

The simultaneous changes in I and $\overline{\theta}$ shown earlier are in accord with a TC evolving close to thermal wind balance. As the moat preceding SEF forms, the region outside of the primary eyewall warms (Fig. 5) as enhanced subsidence occurs there (Fig. 2b). The low-level radial flow $\overline{u}$ outside of the primary eyewall weakens as well (Fig. 2d). Later, as azimuthal-mean rainband heating increases (Figs. 2a,b), SEF occurs. Further physical insight can be gained into these factors by studying the response of a balanced vortex model to fixed latent heating and momentum sources from WRF output.

To address quasi-balanced aspects of SEF, we employ the linearized, nonhydrostatic, anelastic vortex model described in Hodyss and Nolan (2007) and NMS07, now known as 3-Dimensional Vortex Perturbation Analysis and Simulation (3DVPAS). Although the model simulates unsteady nonhydrostatic dynamics, Nolan and Grasso (2003) found that when forced by fixed heat or momentum sources, the steady-state solutions produced by 3DVPAS are an excellent approximation to the response expected from a ''balanced vortex'' model (e.g., Eliassen 1951). This finding has been further verified by comparisons of 3DVPAS output to the analytical solutions of Schubert et al. (2007) and Rozoff et al. (2008) (not shown).

In the current study, the domain for all 3DVPAS calculations covers the radial and height ranges of 0–200 and 0–17.9 km. A staggered Arakawa C-type grid consisting of 211 radial and 69 vertical grid points is used. The radial grid spacing expands outward using the grid stretching described in Nolan and Montgomery (2002) in order to provide higher spatial resolution near the inner core while retaining computational efficiency. The grid spacing is about 0.54 km inside of $r = 37$ km and gently expands to 1.8 km near $r = 200$ km. Grid stretching is employed in the vertical direction as well in order to properly resolve the shallowness of boundary layer friction. Grid spacing is about 0.14 km below 4 km and about 0.4 km near the top of the domain. The time step

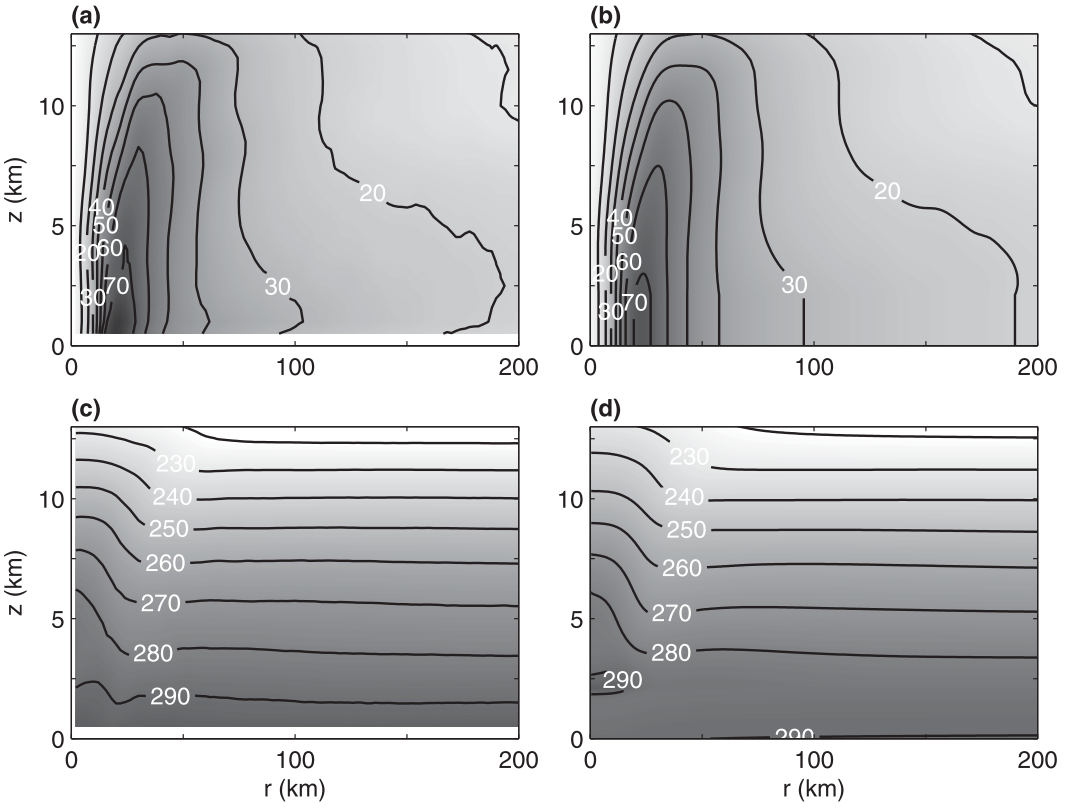

FIG. 8. Radial–height cross sections of the 97-h (a) $\overline{v}$ (m s^{-1}) from WRF, (b) $\overline{v}$ (m s^{-1}) prescribed to 3DVPAS, (c) $\overline{T}$ (K) from WRF, and (d) $\overline{T}$ (K) prescribed to 3DVPAS.

of time integration is 30 s. Steady-state solutions are achieved after about 6 h of simulation time and the balanced responses are obtained from the output at 16 h.

The azimuthal-mean tangential wind from the WRF output is specified in 3DVPAS for our calculations. Figure 8a shows an example of $\overline{v}$ from the WRF simulation at 97 h, near the TC's maximum lifetime intensity. Like many intense TCs, the vortex structure is warm-core, baroclinic, and contains an outward-sloping RMW. Because of friction, winds decay from the top of the boundary layer to the surface. This wind decay can lead to an unrealistic cold anomaly in the boundary layer of 3DVPAS since 3DVPAS refines the basic-state temperature field so that it is in thermal wind balance with the specified wind field. To overstep this complication, the winds at $z = 2$ km are extended with constant values to the surface. In addition, to reduce localized regions of static instability that can be problematic in obtaining balanced response solutions, $\overline{v}$ is smoothed slightly. Figure 8b shows the prescribed $\overline{v}$ field resulting from these procedures. Above $z =$ 2 km, $\overline{v}$ in Fig. 8b is structurally similar to $\overline{v}$ in Fig. 8a. It should be mentioned that while 3DVPAS iteratively seeks a basic state near thermal wind balance, $\overline{T}$ from WRF is specified for the far-field reference state. Except for the lower atmosphere, where a barotropic wind structure is imposed in 3DVPAS, which leads to a lower $\overline{T}$, the structure of $\overline{T}$ is otherwise similar in WRF (Fig. 8c) and 3DVPAS (Fig. 8d).

The latent heating and the azimuthal component of friction from WRF are used to force 3DVPAS. Figures 9a and 9b show $\overline{\dot{\theta}}$ and $\overline{F_\lambda}$ before SEF (105 h), during SEF (115 h), and as the outer eyewall matures (125 h). At 105 h, a single sloping eyewall containing enhanced $\overline{\dot{\theta}}$ is seen at about 20–30-km radius (Fig. 9a). Outside of the eyewall, there is a sloped region of negative $\overline{\dot{\theta}}$ due to melting and evaporation. Farther out ($r \geq 40$ km), positive rainband heating projects onto the azimuthal mean. This region of positive $\overline{\dot{\theta}}$ eventually solidifies into the outer eyewall (115–125 h) while negative $\overline{\dot{\theta}}$ is found in the moat. There is a transient region of positive $\overline{\dot{\theta}}$ in the moat at 125 h due to an asymmetry in the outer eyewall, but this quickly disappears thereafter as the storm acquires a classic double-eyewall structure (i.e., Figs. 1f,g). As for the frictional component of forcing, $\overline{F_\lambda}$ is primarily relevant to the turbulent boundary layer (and therefore only plotted at low levels). It is most significant near the strongest $\overline{v}$. As the winds expand outward from 105 to 125 h, elevated $\overline{F_\lambda}$ shifts outward.

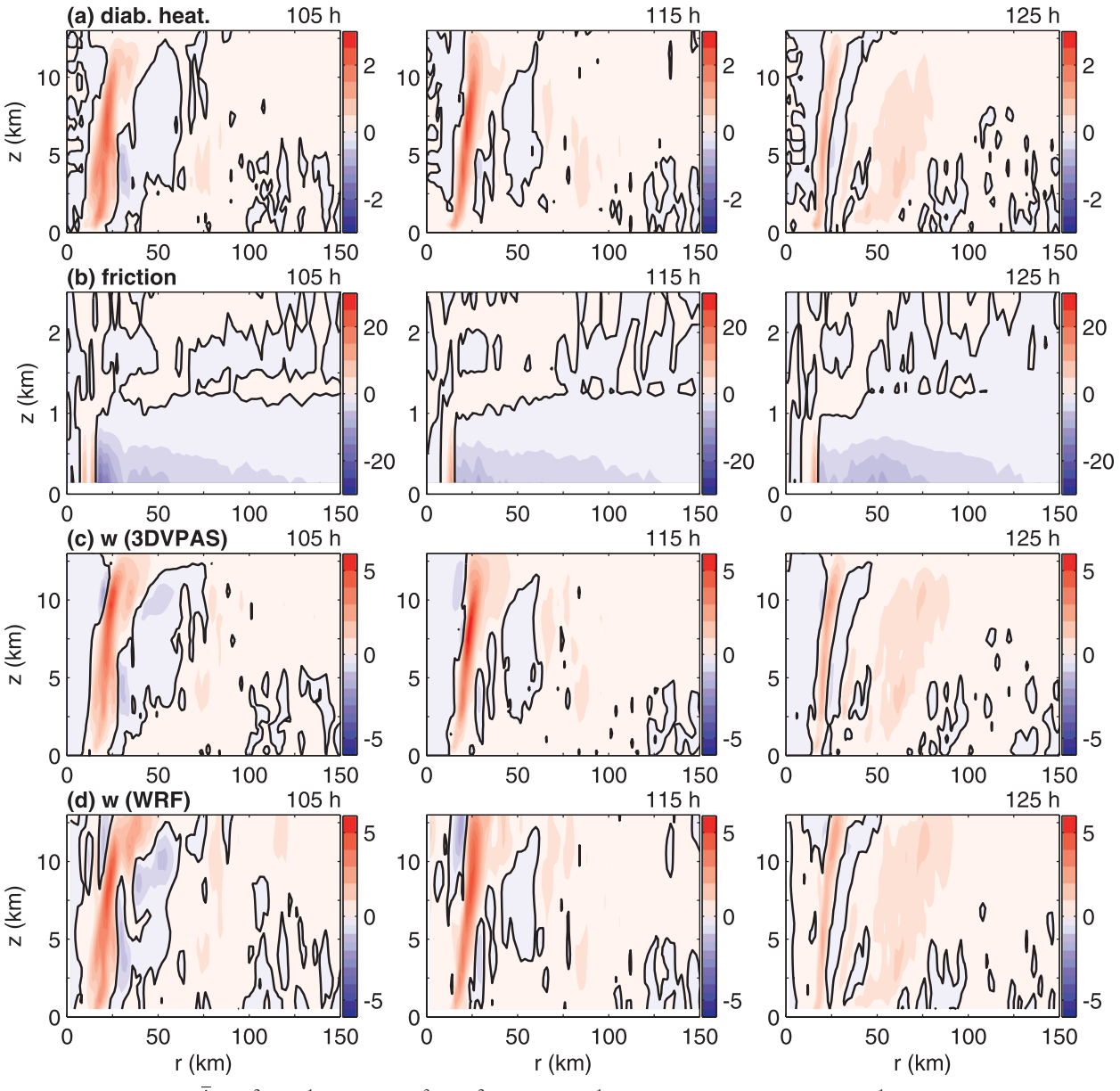

FIG. 9. Shown are (a) $\overline{\dot{\theta}}$ (10^{-2} K s^{-1}), (b) $\overline{F_\lambda}$ (10^{-3} m s^{-2}), (c) $\overline{w}$ (m s^{-1}) from 3DVPAS, and (d) $\overline{w}$ (m s^{-1}) from WRF, all at 105, 115, and 125 h. Note that the vertical scale in (b) is different than in the other rows in order to focus on the boundary layer, where the frictional forcing is most significant.

The steady-state vortex response to stationary forcing from WRF at 105, 115, and 125 h is shown in Fig. 9c. The vertical motion in 3DVPAS mirrors the spatial distribution of $\overline{\dot{\theta}}$, with rising motion in regions of positive $\overline{\dot{\theta}}$ and subsidence in regions of negative $\overline{\dot{\theta}}$. The $\overline{w}$ fields from WRF at corresponding times are provided in Fig. 9d for comparison. There are some differences between 3DVPAS and WRF. In particular, the structure of eye subsidence is wavy in WRF whereas it is quite uniform in 3DVPAS. Also, the overall depth of the $\overline{w}$ maxima and minima in 3DVPAS is not quite as deep as in WRF. Otherwise, there is qualitative agreement in $\overline{w}$ between 3DVPAS and WRF throughout much of the remaining troposphere.

The azimuthal-mean radial component of wind exhibits more discernible differences than $\overline{w}$ in the two models (Fig. 10). The inflow layer in 3DVPAS is deeper and, at times, weaker than in WRF. At 105 h, the minimum value of low-level inflow is -8.6 and -12.5 m s^{-1} in 3DVPAS and WRF, respectively, while at 115 h, the

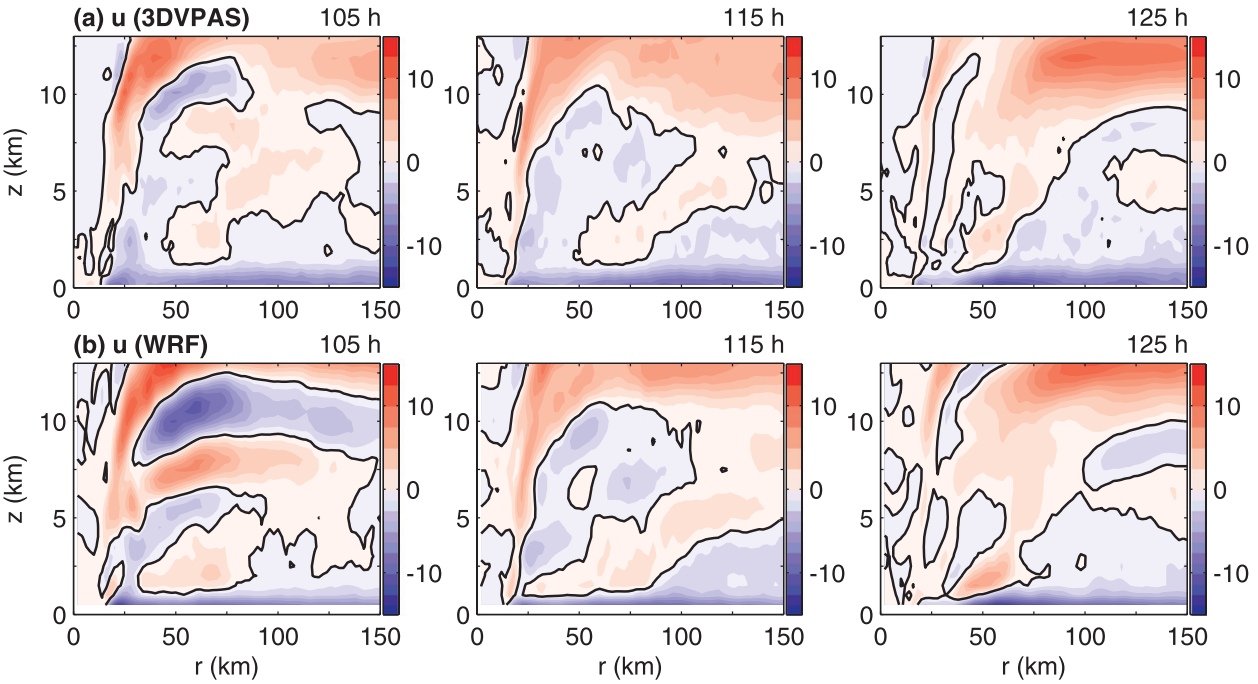

FIG. 10. Shown are $\overline{u}$ (m s^{-1}) from (a) 3DVPAS and (b) WRF at 105, 115, and 125 h.

values are −9.3 and −8.9 m s^{-1}. Both models produce outflow jets just above the boundary layer near the eyewalls, but they are certainly stronger in WRF. Above these outflow jets, there is qualitative agreement between 3DVPAS and WRF, although bands of inflow/outflow are slightly stronger in WRF. The differences between the quasi-balanced and fully simulated transverse circulations in and near the boundary layer were discussed in Bui et al. (2009) and Fudeyasu and Wang (2011). In spite of the differences in vertical structure and magnitude, the low-level inflow in 3DVPAS and WRF share similarities in their radial structure, including the local maxima in low-level inflow near regions of sustained $\overline{\dot{\theta}}$.

Even with the significant simplifications in 3DVPAS, much can be learned about SEF in this idealized framework. As such, we will use 3DVPAS to isolate the roles of diabatic and frictional forcing throughout the SEF process. We will also use 3DVPAS to examine the role of an expanding inertial stability field on SEF.

b. *Relative contributions of forcing to the secondary circulation*

Diabatic and frictional forcing drive a significant portion of the secondary circulation during the SEF process. As such, it is helpful to determine the relative importance of $\overline{\dot{\theta}}$ and $\overline{F_\lambda}$ to the vortex response. Figure 11 shows the relative contributions of $\overline{\dot{\theta}}$ and $\overline{F_\lambda}$ to the response in $\overline{w}$ and $\overline{u}$ at 105 h. (The relative responses at 105 h are quite representative of other times in the WRF simulation.) In terms of $\overline{w}$, the response to $\overline{\dot{\theta}}$ (Fig. 11a) dominates the response to $\overline{F_\lambda}$ (Fig. 11b) by an order of magnitude. The $\overline{w}$ field in Fig. 11a closely resembles the complete response shown in Fig. 9c. The $\overline{F_\lambda}$ forcing imposes a $\overline{w}$ maximum near the top of the boundary layer near the RMW. Gentle lifting exists throughout the depth of the eye. Moreover, the strongest upward motion tilts inward with height. Frictional forcing is expressed more significantly in $\overline{u}$, but primarily in the boundary layer (Fig. 11d). Because $\overline{v}$ trends away from gradient wind balance due to $\overline{F_\lambda}$, gradient wind balance is restored by low-level inflow and an accompanying inward flux of absolute angular momentum. The $\overline{u}$ induced by $\overline{\dot{\theta}}$ occurs throughout the troposphere (Fig. 11c). Also, the inflow occurs over a much deeper layer in Fig. 11c than in Fig. 11d and there are two low-level radial inflow maxima resulting from positive $\overline{\dot{\theta}}$ in those regions. Overall, both $\overline{\dot{\theta}}$ and $\overline{F_\lambda}$ are important in the vortex response.

Examining the vortex response to the positive and negative components of $\overline{\dot{\theta}}$ proves insightful as well. To examine the relative roles of positive and negative $\overline{\dot{\theta}}$, we carry out two additional 3DVPAS experiments that neglect friction at 105 h. The first experiment restricts $\overline{\dot{\theta}}$ to be only nonnegative by zeroing out the negative 105-h $\overline{\dot{\theta}}$ in Fig. 9a. We are left with $\overline{\dot{\theta}}$ associated primarily with the eyewall (Fig. 12a). The response in $\overline{w}$ and $\overline{u}$

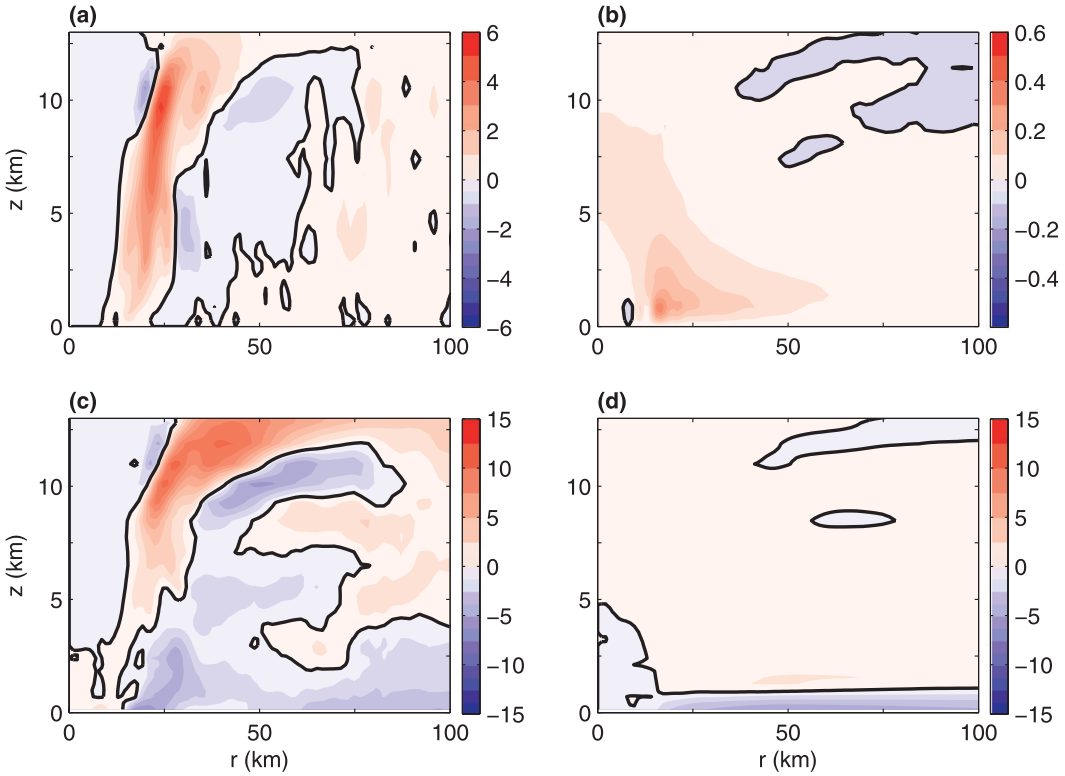

FIG. 11. Vertical wind (m s^{-1}) from 3DVPAS due to (a) $\overline{\dot{\theta}}$ and (b) $\overline{F_\lambda}$. Also shown is $\overline{u}$ (m s^{-1}) from 3DVPAS due to (c) $\overline{\dot{\theta}}$ and (d) $\overline{F_\lambda}$. All panels correspond to 105 h. Also, the contour interval changes from 0.5 to 0.05 m s^{-1} from (a) to (b).

(Figs. 10c,e) is qualitatively similar to the vortex response to the total $\overline{\dot{\theta}}$ field (Figs. 11a,c). In comparison with the response depicted in Figs. 11a and 11c, the moat subsidence is weaker (Fig. 12c) and there is less interruption to the TC's low-level inflow near the moat (Fig. 12e). A second experiment containing only the negative component of $\overline{\dot{\theta}}$ at 105 h explains a significant portion of the moat subsidence and a very small portion of eye subsidence immediately along the inner edge of the primary eyewall (Fig. 12d). The $\overline{u}$ -field response is more complicated (Fig. 12f) but consistent with $\overline{w}$ (Fig. 12d) and mass continuity. Throughout the simulation, moat subsidence is driven by the vortex response to positive $\overline{\dot{\theta}}$ in the eyewalls and rainbands, but it is further enhanced by local cooling associated with precipitation.

c. *The relative importance of forcing and radial structure on balanced aspects of SEF*

To more thoroughly investigate the relative importance of forcing and vortex structure on the spinup of an outer eyewall, we use 3DVPAS for some additional idealized experiments, which are summarized in Table 1. As before, we focus our attention on the times of 105, 115, and 125 h because they represent key points of evolution during SEF. At 105 h, the rainband activity in the region of eventual SEF is just starting to increase outside of the primary eyewall and the wind field expands rapidly thereafter, yielding an increase in the kinetic energy (Figs. 6 and 7). At 115 h, SEF starts to become apparent in multiple fields (Fig. 2). By 125 h, SEF has nearly completed and a double eyewall structure is just becoming evident in horizontal plots of synthetic radar reflectivity. We only present three snapshots in time since 3DVPAS calculations for times in between show congruous results.

Our primary interest here is to understand the WRF's spinup of the outer eyewall within the idealized framework. To this end, we use 3DVPAS to diagnose symmetric tangential wind tendencies $\overline{v_t}$ in response to symmetric forcing and vortex structure at 105, 115, and 125 h. These three experiments are denoted as the control experiments C1, C2, and C3 (Table 1). The details of the diagnosed transverse circulation for these times were examined in the previous section in Figs. 9 and 10. Denoting 105 h as a reference time, some additional sensitivity experiments are carried out as well, allowing us to isolate the impact of changes to the distribution of diabatic ($\overline{\dot{\theta}}$) and frictional ($\overline{F_\lambda}$) forcing and

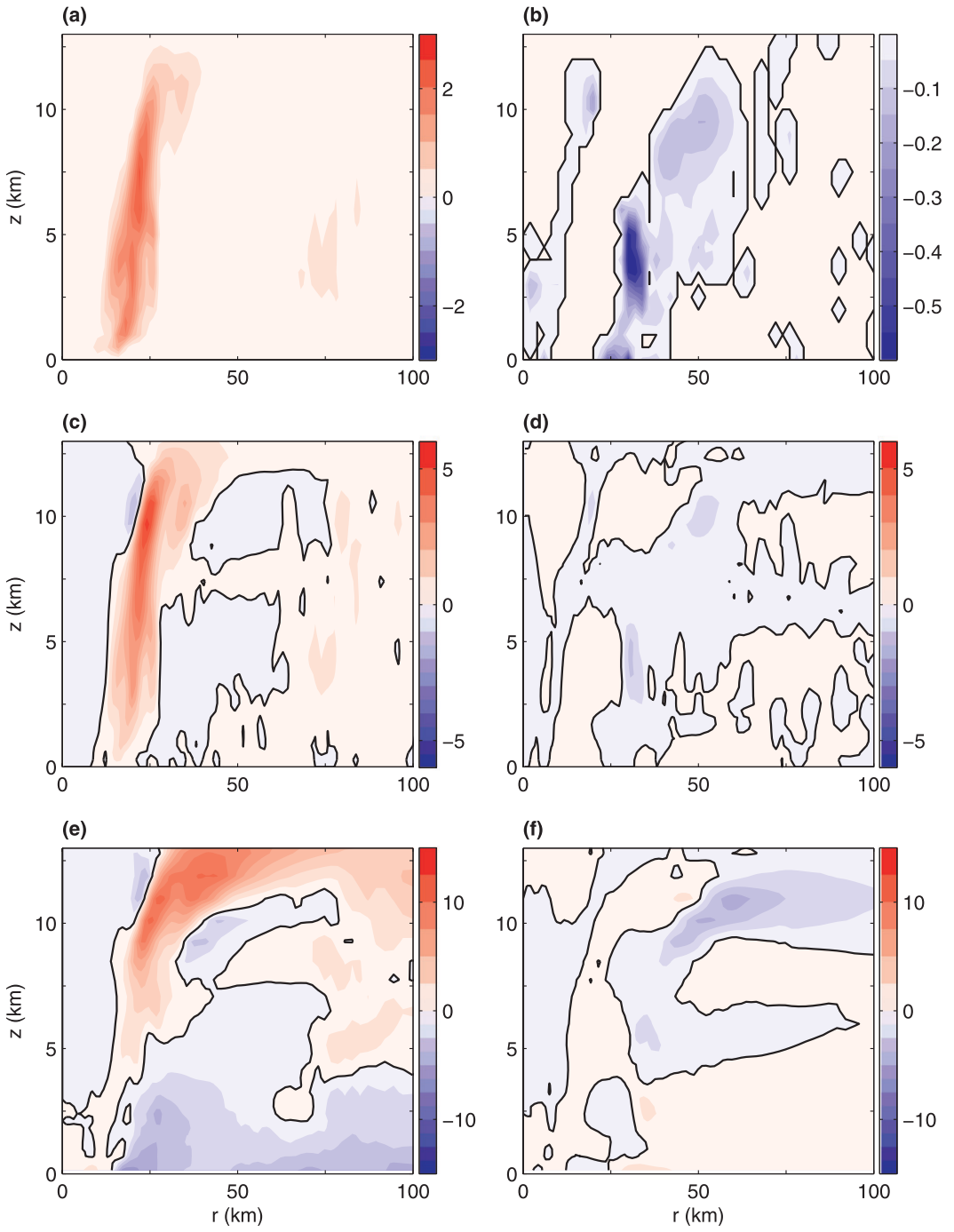

FIG. 12. (a) Positive and (b) negative $\bar{\theta}$ from WRF at 105 h, in which $\bar{\theta}$ is shaded at intervals of 0.25×10^{-2} and 0.05×10^{-2} K s^{-1}. (c),(d) The 3DVPAS $\overline{w}$ (m s^{-1}) resulting from the $\bar{\theta}$ in (a) and (b), respectively. (e),(f) The 3DVPAS $\overline{u}$ (m s^{-1}) resulting from the $\bar{\theta}$ in (a) and (b), respectively.

changes to the $\overline{v}$ and $\overline{T}$ structure. These experiments, which are denoted E1, E2, E3, and E4, are also described in Table 1. As an example, E1 shows the impact of an expanded vortex structure at 115 h (i.e., the time of SEF) on the TC response to forcing at 105 h.

Before more thoroughly examining the specific vortex response to changes in vortex structure and forcing, we review changes in the vortex structure that are relevant to traditional Eliassen-type balanced vortex calculations. Important structural parameters include the inertial stability

TABLE 1. A summary of 3DVPAS experiments and corresponding descriptions of the times when the prescribed azimuthal-mean tangential wind $\overline{v}$ and temperature $\overline{T}$ and the diabatic heating $\overline{\dot{\theta}}$ and friction $\overline{F_\lambda}$ forcing terms were chosen from WRF.

Experiment name	Description
C1	$\overline{v}$, $\overline{T}$ at 105 h and $\overline{\dot{\theta}}$, $\overline{F_\lambda}$ at 105 h
C2	$\overline{v}$, $\overline{T}$ at 115 h and $\overline{\dot{\theta}}$, $\overline{F_\lambda}$ at 115 h
C3	$\overline{v}$, $\overline{T}$ at 125 h and $\overline{\dot{\theta}}$, $\overline{F_\lambda}$ at 125 h
E1	$\overline{v}$, $\overline{T}$ at 115 h and $\overline{\dot{\theta}}$, $\overline{F_\lambda}$ at 105 h
E2	$\overline{v}$, $\overline{T}$ at 125 h and $\overline{\dot{\theta}}$, $\overline{F_\lambda}$ at 105 h
E3	$\overline{v}$, $\overline{T}$ at 105 h and $\overline{\dot{\theta}}$, $\overline{F_\lambda}$ at 115 h
E4	$\overline{v}$, $\overline{T}$ at 105 h and $\overline{\dot{\theta}}$, $\overline{F_\lambda}$ at 125 h

and the static stability, the latter of which will be denoted by the Brunt–Väisälä frequency $N = [(g/\overline{\theta})(\partial\overline{\theta}/\partial z)]^{1/2}$. Baroclinity is also relevant to balanced vortex calculations as well, but inertial and static stabilities tend to dominate the behavior of solutions over most of the domain, so our focus here is on I and N. Figure 13a shows that, at 105 h (i.e., C1), the distribution of I decays smoothly outside of a core of elevated I ($r \leq 25$ km), consistent with a modified Rankine vortex structure (e.g., Mallen et al. 2005). As SEF takes place between 115 and 125 h (Fig. 13a), I decreases in the eye and inner eyewall ($r \leq 25$ km) as the winds subside in the inner eyewall. As expected during an ERC, I increases outside of the inner eyewall and especially in the region of the developing outer eyewall. Figure 13b shows the accompanying distribution of N at 105 h and its changes from that time to 115 and 125 h. The warm-core structure and eye inversion impose enhanced layers of N in the eye at 105 h. Relatively low N exists outside of the eyewall, especially at mid- to upper levels. The ensuing changes to N are somewhat complex and layerwise by 115 h, but by 125 h there is a more noteworthy general increase to static stability in the moat region and beyond ($r \geq 25$ km and $5.0 \leq z \leq 11$ km). The impact of these structural changes will be demonstrated in the following results.

Figure 14a shows the diagnosis of $\overline{v_t}$ in the control experiments C1, C2, and C3, which show the vortex response to the vortex structure and total forcing at 105, 115, and 125 h. It should be noted these values of $\overline{v_t}$ in C1 through C3 will generally not quantitatively match those seen in WRF because of the neglect of unbalanced aspects of the flow in the boundary layer, but the diagnosed $\overline{v_t}$ illustrate how TC structure changes affect the efficiency of $\overline{\dot{\theta}}$ in vortex intensification. The $\overline{v_t}$ response is highest near the primary eyewall at 105 and 115 h and near both the inner and developing outer eyewall at 125 h. Immediately outside of the primary eyewall, there are negative $\overline{v_t}$ at lower levels, which, as confirmed with experiments that individually isolate the $\overline{\dot{\theta}}$ and $\overline{F_\lambda}$, turn out to be a consequence of $\overline{F_\lambda}$ (not shown). As we progress in time from C1 to C3, positive $\overline{v_t}$ near the surface increases in the vicinity of the developing and contracting outer eyewall, which is roughly located

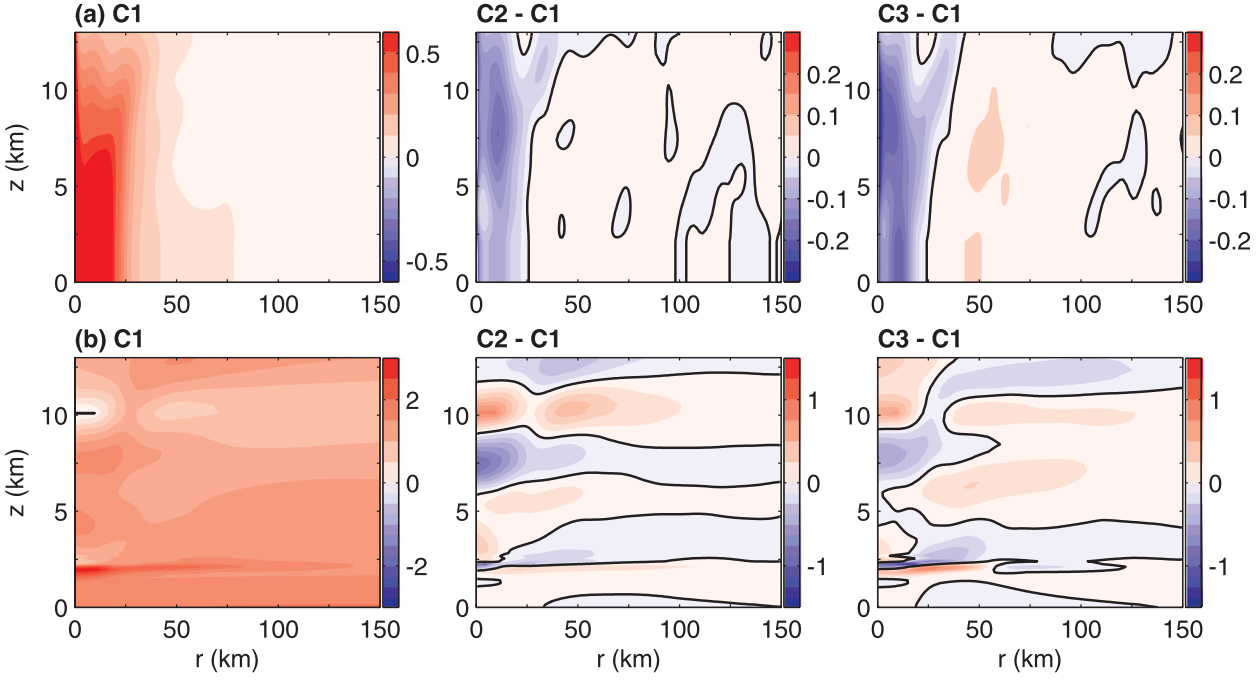

FIG. 13. (a) Inertial stability (10^{-2} s^{-1}) at 105 h (C1) and changes in I from 105 to 115 h (C2 − C1) and from 105 to 125 h (C3 − C1). (b) Static stability (10^{-2} s^{-1}) at 105 h (C1) and changes in N from 105 to 115 h (C2 − C1) and from 105 to 125 h (C3 − C1).

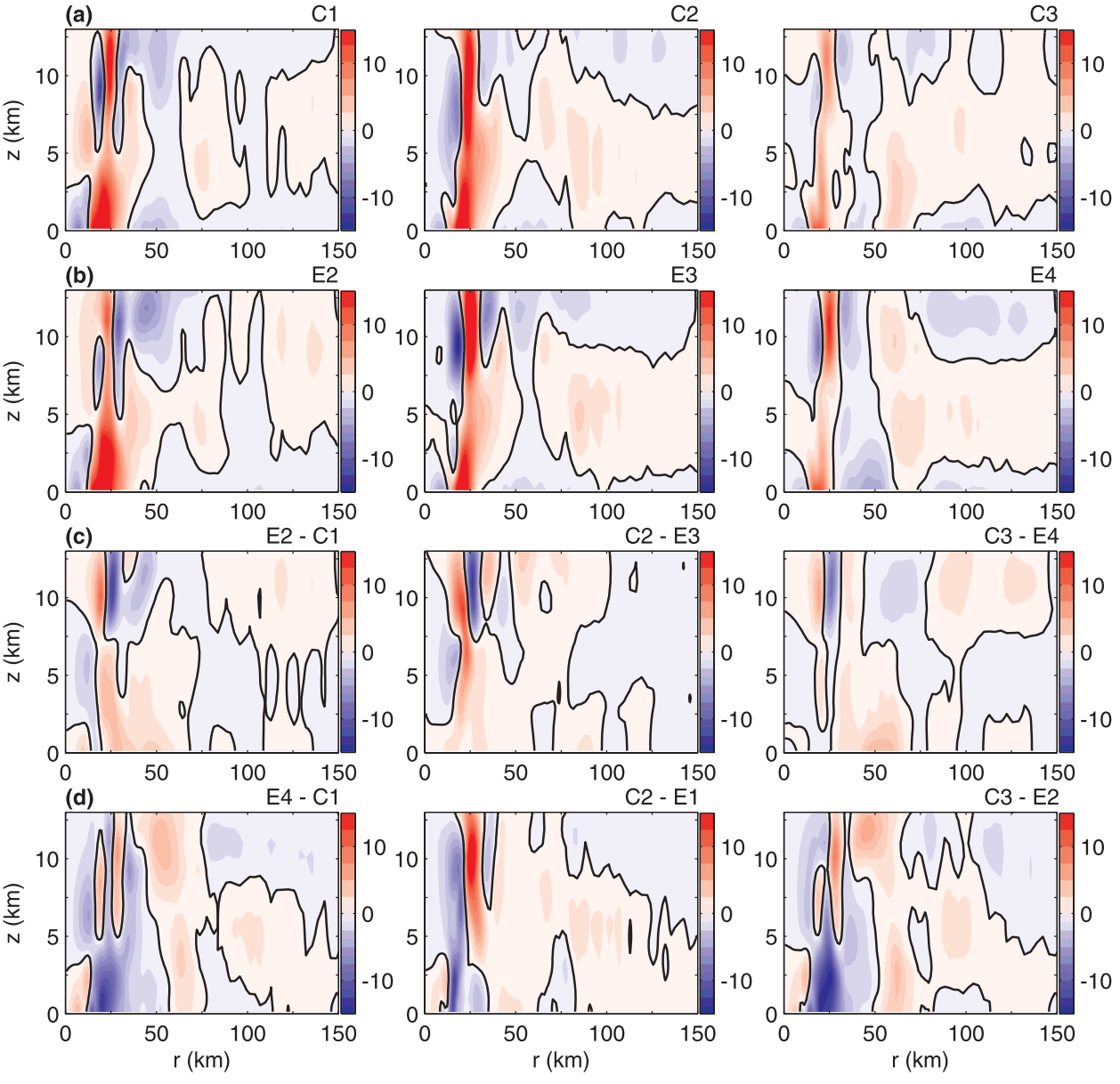

FIG. 14. (a) A diagnosis of $\overline{v}_t$ (m s^{-1} h^{-1}) in experiments C1, C2, and C3, and (b) $\overline{v}_t$ in experiments E2, E3, and E4. (c): Difference fields of $\overline{v}_t$ (m s^{-1} h^{-1}) showing the impact of changing vortex structure, including differences between E2 and C1, C2 and E3, and C3 and E4. (d) Difference fields of $\overline{v}_t$ (m s^{-1} h^{-1}) showing the impact of changing forcing, including differences between E4 and C1, C2 and E1, and C3 and E2.

between 60 and 100 km at 115 h and between 40 and 60 km at 125 h (see Fig. 9).

Experiments E1 and E2 include the vortex structure at 115 and 125 h while using forcing from 105 h, while experiments E3 and E4 use forcing from 115 and 125 h with a vortex structure fixed at 105 h. Because the results in E1 are similar to E2, $\overline{v}_t$ from E1 is not shown in Fig. 14. Overall, Fig. 14b shows that the overall structure of $\overline{v}_t$ in E2, E3, and E4 resembles the structure in C1, C2, and C3, respectively, but there are quantitative differences. Figures 14c and 14d show a variety of difference fields to emphasize the relative impacts of changing vortex structure and forcing on $\overline{v}_t$. For example, Fig. 14c shows difference fields that show how the change in vortex structure impacts the response to fixed heating. The difference field of $\overline{v}_t$ between E2 and C1 shows that changing the vortex structure from 105 to 125 h with fixed 105-h forcing yields a substantial positive increase in low- to midlevel $\overline{v}_t$ over a large region extending from the inner eyewall out to nearly 75 km. On the other hand, as seen in the difference fields C2 − E3 and C3 − E4, using either a fixed forcing at 115 or 125 h while allowing

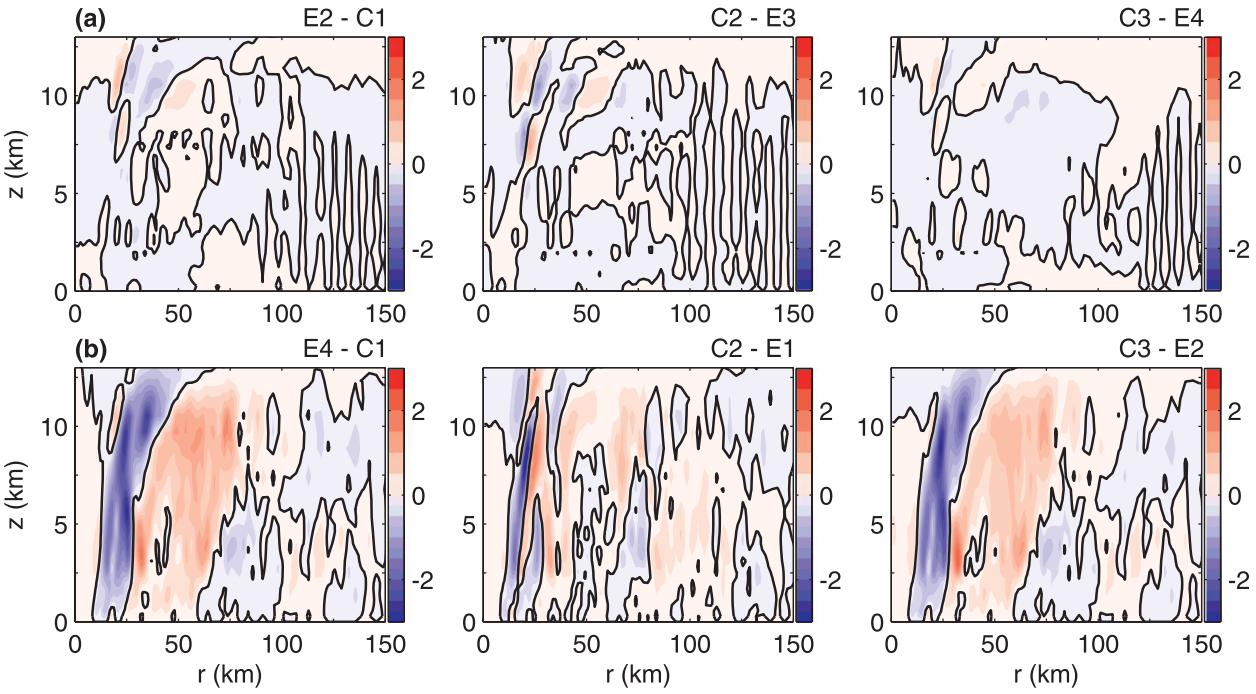

FIG. 15. (a) Difference fields of $\overline{w}$ (m s^{-1}) showing the impact of changing vortex structure, including differences between E2 and C1, C2 and E3, and C3 and E4. (b) Difference fields of $\overline{w}$ (m s^{-1}) showing the impact of changing forcing, including differences between E4 and C1, C2 and E1, and C3 and E2.

the vortex structure to change from 105 h to either 115 or 125 h, respectively, yields a more substantial increase in the low-level winds in the vicinity of the incipient outer eyewall's latent heating. This increase accelerates in time, suggesting the region near the outer eyewall is becoming more efficient at retaining latent heat energy as kinetic energy. (Note, a difference field given by E1 − C1 is so similar to E2 − C1 that it is not shown.)

The difference fields provided in Fig. 14d emphasize the impact of forcing on $\overline{v_t}$. The difference between $\overline{v_t}$ in E4 and C1 shows that changing the forcing from 105 to 125 h with a fixed 105-h vortex structure substantially decreases $\overline{v_t}$ near the inner eyewall and moat while $\overline{v_t}$ is increased on the outer edge of the outer eyewall heating. The remaining difference fields shown in Fig. 14d show the impact of fixing the vortex structure at either 115 h (C2 − E1) or 125 h (C3 − E2) and allowing the forcing to vary between 105 h and either 115 or 125 h, respectively. Once again, positive $\overline{v_t}$ is seen near the outer eyewall region, but it is more restricted to the outer edge of the eyewall and substantially smaller at low levels in the center of the developing outer eyewall. Overall, these results show that both the forcing and expanding wind field contribute to the expansion of the wind field. Both increasingly contribute to enhanced $\overline{v_t}$ in time as the outer eyewall intensifies and contracts. However, in both the early and later stages of SEF, the impact of the expanding wind field is actually more dominant in the $\overline{v_t}$ response within the lower levels of the incipient outer eyewall, while forcing is more effective at spinning up the winds at mid- to upper levels.

To understand why the expanding wind field contributes to SEF in the balanced framework, we now consider the diagnosed transverse circulation associated with each experiment. We recall that Figs. 9 and 10 show the secondary circulations for C1, C2, and C3. The secondary circulations in experiments E1–E4 actually look qualitatively similar to C1–C3, so it is more illustrative to just consider the associated difference fields of $\overline{w}$ and $\overline{u}$. Figure 15 shows the difference fields for $\overline{w}$ corresponding to the difference fields of $\overline{v_t}$ shown in Figs. 14c and 14d. Once again, Fig. 15a exemplifies the impact of changing the vortex structure on $\overline{w}$ associated with fixed $\overline{\dot{\theta}}$ and $\overline{F_\lambda}$. In the inner eyewall, there are some lateral shifts in the upper-level updraft associated with the changing structure of N (see Fig. 13b), particularly in E2 − C1 and C2 − E3. However, the overall magnitude of $\overline{w}$ changes is small elsewhere. Nonetheless, even though $\overline{F_\lambda}$ is fixed in each difference field in Fig. 15a, there is a slight increase in upward motion at low levels outside of 50-km radius in E2 − C1 and C3 − E4 (which show the impact of the change in vortex structure from 105 to 125 h). This increased low-level lift corresponds to increased low-level horizontal convergence (not

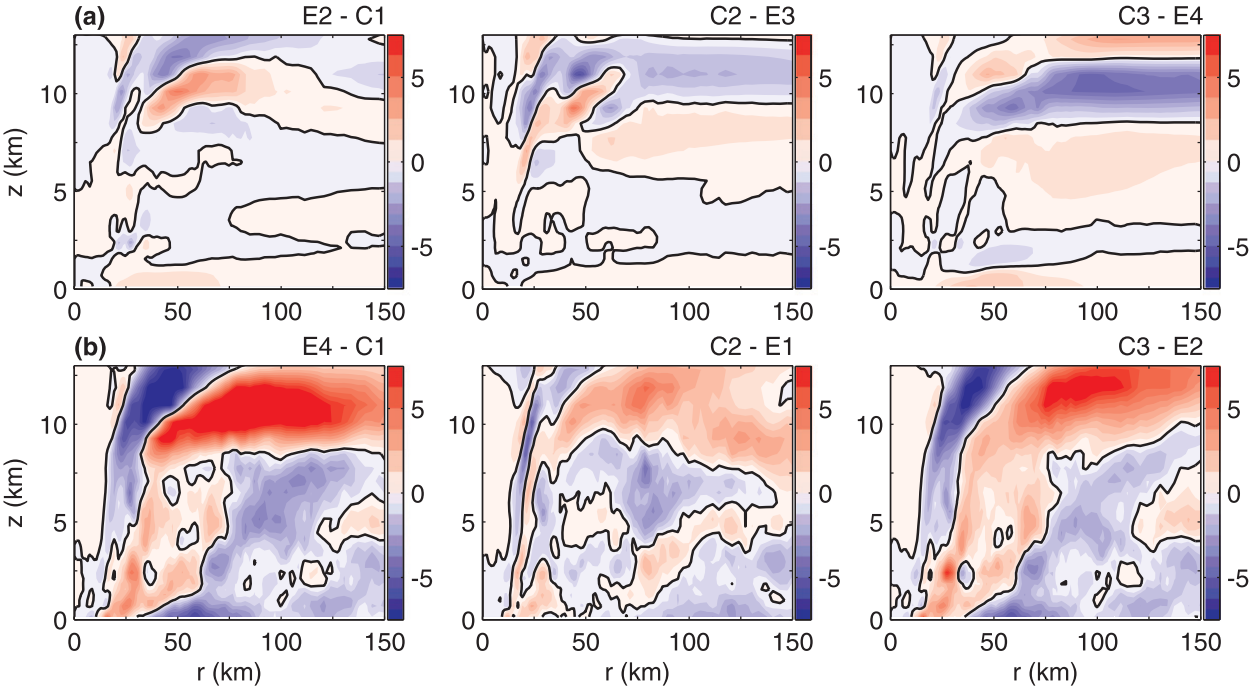

FIG. 16. (a) Difference fields of $\overline{u}$ (m s^{-1}) showing the impact of changing vortex structure, including differences between E2 and C1, C2 and E3, and C3 and E4. (b) Difference fields of $\overline{u}$ (m s^{-1}) showing the impact of changing forcing, including differences between E4 and C1, C2 and E1, and C3 and E2.

shown). Also, there is enhanced subsidence or less upward motion over a broad midlevel region encompassing the moat and outer eyewall for $\dot{\theta}$ and $\overline{F_\lambda}$ fixed at 125 h (i.e., C3 − E4), consistent with increasing N and also the results in Rozoff et al. (2008) showing that increasing I enhances local moat subsidence in between concentric rings of diabatic heating. Now, the $\overline{w}$ response produced by changing the distribution of $\dot{\theta}$ and $\overline{F_\lambda}$ is quite dramatic (Fig. 15b). The difference fields E4 − C1 and C3 − E2 clearly show a large outward shift of $\overline{w}$ between 105 and 125 h because the $\dot{\theta}$ (and low-level linear Ekman pumping associated with $\overline{F_\lambda}$) is shifted outward with an outer eyewall emerging between experiments C1 and E4. Likewise, the weakened inner eyewall shows up as strongly negative values of $\overline{w}$. Similar circulation shifts are evident in going from 105 to 115 h (e.g., C2 − E1).

Figure 16 shows difference fields of $\overline{u}$ for the same experiments. These results are perhaps most informative in interpreting the increasing efficiency of outer eyewall development. First, the changing vortex structure (Fig. 16a) leads to a vertical shift in the upper-level outflow. For example, the vertical shift of the outflow channel shown in C3 − E4 is consistent with the outward shift of enhanced midlevel static and inertial stability. Enhanced inertial stability associated with the expanding wind field also substantially decreases the low-level inflow, especially at 125 h. This explains the stronger low-level upward motion outside of 50-km radius seen in Fig. 15a. Compared to the changing vortex structure, the evolving distribution of $\dot{\theta}$ and $\overline{F_\lambda}$ associated with SEF has a more dramatic impact on the $\overline{u}$ component of the vortex response (Fig. 16b). Keeping the vortex structure fixed but shifting the eyewall $\dot{\theta}$ associated with the expanded wind field from a single to double eyewall structure and shifting the $\overline{F_\lambda}$ associated with the expanding wind field creates greater inflow into the developing outer eyewall.

Even though the experiments that shift forcing outward produce stronger increases in low-level inflow near the nascent outer eyewall, the low-level $\overline{v_t}$ associated with SEF is higher in the experiments allowing vortex structure to expand outward. From (1), it can easily be shown that $\overline{v_t}$ is related to the radial flux of absolute vorticity $-\overline{u}\overline{\zeta_a}$. This quantity helps explain the low-level patterns in $\overline{v_t}$, while the vertical advection term in the equation for $\overline{v_t}$ (not shown) helps explain midlevel $\overline{v_t}$ patterns. Difference fields corresponding to earlier figures are shown for this quantity in Fig. 17. As in the difference fields for $\overline{v_t}$, the low-level vorticity flux is enhanced in the region of the incipient outer eyewall. In the experiments that fix forcing but vary vortex structure, there is a strong vorticity flux in the region of SEF. This flux is generally stronger than the vorticity flux resulting from the changes in forcing, which also tends to be located more on the outer edge of the developing outer

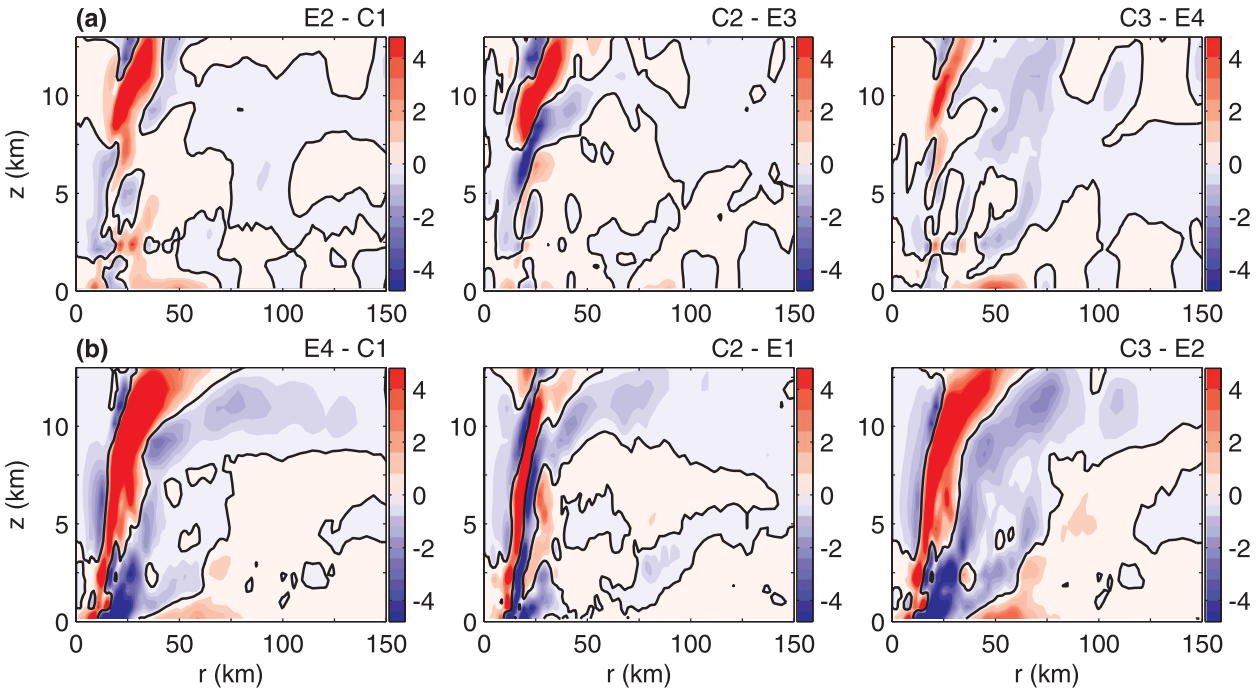

FIG. 17. (a) Difference fields of $-\overline{u}\overline{\zeta_a}$ ($\times 10^{-3}$ m s^{-2}) showing the impact of changing vortex structure, including differences between E2 and C1, C2 and E3, and C3 and E4. (b) Difference fields of $-\overline{u}\overline{\zeta_a}$ ($\times 10^{-3}$ m s^{-2}) showing the impact of changing forcing, including differences between E4 and C1, C2 and E1, and C3 and E2.

eyewall. In essence, the enhanced inertial stability associated with an expanding vortex structure is associated with enhanced absolute vorticity. Therefore, even though the low-level inflow is weakened in Fig. 17a, the larger vorticity more than compensates in the equation for $\overline{v}_t$, yielding even greater values of $\overline{v}_t$ than in the stronger low-level inflow driven by changes to forcing alone. Nonetheless, it is important to point out that the changing distribution of diabatic and frictional forcing is quite substantial to the development of the outer eyewall as well.

6. Conclusions

Axisymmetric aspects of secondary eyewall formation (SEF) are revisited using an idealized, cloud-resolving WRF simulation on the β plane. SEF rapidly commences as soon as rainband latent heating outside of the primary eyewall substantially projects onto the azimuthal-mean state. These rainbands are likely enhanced by the TC-induced β shear as described in FZ12 and convective development in these bands near the site of SEF may be further enhanced by the frontlike structure that appears in fields of equivalent potential temperature. The radial extent and intensity of the azimuthal-mean latent heating abruptly increases as soon as the simulated SEF event begins. This heating is sustained during the subsequent ERC. Absolute angular momentum, kinetic energy, and attendant inertial stability expand radially as the outer eyewall matures and contracts inward. The kinetic energy efficiency of the outer eyewall region of the TC steadily increases in turn.

An axisymmetric, linearized, nonhydrostatic vortex model is used to diagnose the secondary circulation corresponding to the azimuthal-mean tangential wind and the azimuthal-mean latent heating and friction from WRF. These numerical solutions lack some unbalanced aspects of SEF, but they provide insight into the importance of the vortex structure and forcing on SEF. The idealized solutions for the secondary circulation are qualitatively similar to the mean secondary circulation produced in WRF. In this framework, as the wind field expands in response to rainband latent heating, the low-level inflow decreases near the inner eyewall and increases in the vicinity of rainband heating. These aspects of the vortex response, which precede SEF by several hours, are consistent with a number of other recent studies (e.g., Bui et al. 2009; Xu and Wang 2010b; Fudeyasu and Wang 2011; HMW12).

Using the balanced vortex model, sensitivity experiments were carried out throughout an SEF event to isolate and quantify the relative impacts of the changes in forcing and inertial stability in the generation of the outer eyewall in the WRF. The essence of these results is that, in the vicinity of the incipient outer eyewall, an expansion of

the inertial stability is more efficient in the intensification of the low-level winds than increasing diabatic heating and frictional forcing. To be clear, however, the outward shift in heating and Ekman pumping are essential to the spinup of an outer eyewall as well. In essence, there is a positive feedback suggested here, where an expanding wind field increases the efficiency of the vortex spinup associated with latent heating. Increased Ekman pumping associated with expanding friction facilitates more convection, which yields continued growth of the outer eyewall. While these results are derived from applying an idealized model to WRF output, the importance of both inertial stability and forcing in SEF are expected to remain relevant in more realistic models that account for nonlinear boundary layer dynamics in SEF (e.g., HMW12). Also, while these concepts should be further examined in analyses accounting for asymmetric dynamics, it is anticipated that these symmetric concepts will still play an essential role.

The angular momentum budget calculations in this study indicate that any forcing mechanism that produces sufficiently strong and sustained latent heating outside of the primary eyewall will promote SEF. These results support recent studies showing how higher values of relative humidity (Hill and Lackmann 2009), rainband diabatic heating (Wang 2009), surface moist enthalpy flux in the outer core (Xu and Wang 2010a), and initial vortex size (Xu and Wang 2010b) are effective means to increasing the size of a TC via the expansion of the wind field and resulting boundary layer inflow. The results ultimately confirm the relevance of the pioneering results of SW82, SH82, and HS86 as well, but they do so using more realistic evolving distributions of inertial stability and forcing—namely, in cases where a TC has a more expansive wind field, not only will the frictional inflow be enhanced, but the inertial stability will be higher as well, which will more readily support the development of an outer eyewall should latent heating activity persist in this region. It would be interesting to study large observational datasets or many model simulations to see if there is a way to anticipate the likelihood and location of SEF based on the distribution of low-level inertial stability and diabatic heating.

In a way, the role of the radial structure of inertial stability in SEF shares some similarities with the BSA mechanism proposed in Terwey and Montgomery (2008). Akin to the organizing properties of the β skirt in the BSA mechanism, the enhanced inertial stability field accompanying a more expansive β skirt increases the rainband organization and its impact on SEF. In either viewpoint, attainable convective instability and the WISHE mechanism important for the latent heat release needed for SEF should be required.

Acknowledgments. We thank Matthew Sitkowski and Daniel Stern for helpful discussions that benefitted this work. We gratefully acknowledge Chun-Chieh Wu and two anonymous reviewers for outstanding critical reviews of this manuscript that led to significant improvements. C. Rozoff was supported by ONR Grant N00014-07-1-0163 and NOAA Grants NA06NES4400002 and NA10NES 4400013. D. Nolan was supported in part by NSF Grant ATM-0756308. F. Zhang was supported by ONR Grant N000140910526, NOAA HFIP, and NSF Grant 0840651. J. Fang was supported by the Nature Science Foundation of China Grants 40921160382 and 40830958, and State Key Basic Program of China 2009CB421502. The WRF simulation was carried out at the Texas Advanced Computing Center.

REFERENCES

Abarca, S. F., and K. L. Corbosiero, 2011: Secondary eyewall formation in WRF simulations of hurricanes Rita and Katrina (2005). *Geophys. Res. Lett.,* **38,** L07802, doi:10.1029/2011GL047015.

Bui, H. H., R. K. Smith, M. T. Montgomery, and J. Peng, 2009: Balanced and unbalanced aspects of tropical cyclone intensification. *Quart. J. Roy. Meteor. Soc.,* **135,** 1715–1731.

Chen, H., D.-L. Zhang, J. Carton, and R. Atlas, 2011: On the rapid intensification of Hurricane Wilma (2005). Part I: Model prediction and structural changes. *Wea. Forecasting,* **26,** 885–901.

Didlake, A. C., and R. A. Houze, 2011: Kinematics of the secondary eyewall observed in Hurricane Rita (2005). *J. Atmos. Sci.,* **68,** 1620–1636.

Eliassen, A., 1951: Slow thermally or frictionally controlled meridional circulation in a circular vortex. *Astrophys. Norv.,* **5,** 19–60.

Fang, J., and F. Zhang, 2012: Effect of beta shear on simulated tropical cyclones. *Mon. Wea. Rev.,* in press.

Fudeyasu, H., and Y. Wang, 2011: Balanced contribution to the intensification of a tropical cyclone simulated in TCM4: Outer-core spinup process. *J. Atmos. Sci.,* **68,** 430–449.

Guinn, T. A., and W. H. Schubert, 1993: Hurricane spiral bands. *J. Atmos. Sci.,* **50,** 3380–3403.

Hack, J. J., and W. H. Schubert, 1986: Nonlinear response of atmospheric vortices to heating by organized cumulus convection. *J. Atmos. Sci.,* **43,** 1559–1573.

Hill, K. A., and G. M. Lackmann, 2009: Influence of environmental humidity on tropical cyclone size. *Mon. Wea. Rev.,* **137,** 3294–3315.

Hodyss, D., and D. S. Nolan, 2007: Linear anelastic equations for atmospheric vortices. *J. Atmos. Sci.,* **64,** 2947–2959.

Hogsett, W., and D.-L. Zhang, 2009: Numerical simulation of Hurricane Bonnie (1998). Part III: Energetics. *J. Atmos. Sci.,* **66,** 2678–2696.

Hong, S.-Y., J. Dudhia, and S.-H. Chen, 2004: A revised approach to ice microphysical processes for the parameterization of clouds and precipitation. *Mon. Wea. Rev.,* **132,** 103–120.

Huang, Y.-H., M. T. Montgomery, and C.-C. Wu, 2012: Concentric eyewall formation in Typhoon Sinlaku (2008). Part II: Axisymmetric dynamical processes. *J. Atmos. Soc.,* **69,** 662–674.

Jordan, C. L., 1958: Mean soundings for the West Indies area. *J. Meteor.,* **15,** 91–97.

Judt, F., and S. S. Chen, 2010: Convectively generated potential vorticity in rainbands and formation of the secondary eyewall in Hurricane Rita of 2005. *J. Atmos. Sci.,* **67,** 3581–3599.

Kossin, J. P., and M. Sitkowski, 2009: An objective model for identifying secondary eyewall formation in hurricanes. *Mon. Wea. Rev.,* **137,** 876–892.

Kuo, H.-C., L.-Y. Lin, C.-P. Chang, and R. T. Williams, 2004: The formation of concentric vorticity structures in typhoons. *J. Atmos. Sci.,* **61,** 2722–2734.

——, W. H. Schubert, C.-L. Tsai, and Y.-F. Kuo, 2008: Vortex interactions and barotropic aspects of concentric eyewall formation. *Mon. Wea. Rev.,* **136,** 5183–5198.

Maclay, K. S., M. DeMaria, and T. H. Vonder Haar, 2008: Tropical cyclone inner-core kinetic energy evolution. *Mon. Wea. Rev.,* **136,** 4882–4898.

Mallen, K. J., M. T. Montgomery, and B. Wang, 2005: Reexamining the near-core radial structure of the tropical cyclone primary circulation: Implications for vortex resiliency. *J. Atmos. Sci.,* **62,** 408–425.

Martinez, Y., G. Brunet, and M. K. Yau, 2010: On the dynamics of two-dimensional hurricane-like concentric rings vortex formation. *J. Atmos. Sci.,* **67,** 3253–3268.

——, ——, ——, and X. Wang, 2011: On the dynamics of concentric eyewall genesis: Space–time empirical normal modes diagnosis. *J. Atmos. Sci.,* **68,** 457–476.

Montgomery, M. T., and R. J. Kallenbach, 1997: A theory for vortex Rossby-waves and its application to spiral bands and intensity changes in hurricanes. *Quart. J. Roy. Meteor. Soc.,* **123,** 435–465.

Moon, Y., and D. S. Nolan, 2010: The dynamic response of the hurricane wind field to spiral rainband heating. *J. Atmos. Sci.,* **67,** 1779–1805.

——, ——, and M. Iskandarani, 2010: On the use of two-dimensional incompressible flow to study secondary eyewall formation in tropical cyclones. *J. Atmos. Sci.,* **67,** 3765–3773.

Noh, Y., W.-G. Cheon, S.-Y. Hong, and S. Raasch, 2003: Improvement of the K-profile model for the planetary boundary layer based on large eddy simulation data. *Bound.-Layer Meteor.,* **107,** 401–427.

Nolan, D. S., 2007: What is the trigger for tropical cyclogenesis? *Aust. Meteor. Mag.,* **56,** 241–266.

——, and M. T. Montgomery, 2002: Nonhydrostatic, three-dimensional perturbations to balanced, hurricane-like vortices. Part I: Linearized formulation, stability, and evolution. *J. Atmos. Sci.,* **59,** 2989–3020.

——, and L. D. Grasso, 2003: Nonhydrostatic, three-dimensional perturbations to balanced, hurricane-like vortices. Part II: Symmetric response and nonlinear simulations. *J. Atmos. Sci.,* **60,** 2717–2745.

——, Y. Moon, and D. P. Stern, 2007: Tropical cyclone intensification from asymmetric convection: Energetics and efficiency. *J. Atmos. Sci.,* **64,** 3377–3405.

Nong, S., and K. Emanuel, 2003: A numerical study of the genesis of concentric eyewalls in hurricanes. *Quart. J. Roy. Meteor. Soc.,* **129,** 3323–3338.

Qiu, X., Z.-M. Tan, and Q. Xiao, 2010: The roles of vortex Rossby waves in hurricane secondary eyewall formation. *Mon. Wea. Rev.,* **138,** 2092–2109.

Ritchie, E. A., and W. M. Frank, 2007: Interactions between simulated tropical cyclones and an environment with a variable Coriolis parameter. *Mon. Wea. Rev.,* **135,** 1889–1905.

Rotunno, R., and K. A. Emanuel, 1987: An air–sea interaction theory for tropical cyclones. Part II: Evolutionary study using a nonhydrostatic axisymmetric numerical model. *J. Atmos. Sci.,* **44,** 542–561.

Rozoff, C. M., W. H. Schubert, and J. P. Kossin, 2008: Some dynamical aspects of tropical cyclone concentric eyewalls. *Quart. J. Roy. Meteor. Soc.,* **134,** 583–593.

Schubert, W. H., and J. J. Hack, 1982: Inertial stability and tropical cyclone development. *J. Atmos. Sci.,* **39,** 1687–1697.

——, C. M. Rozoff, J. L. Vigh, B. D. McNoldy, and J. P. Kossin, 2007: On the distribution of subsidence in the hurricane eye. *Quart. J. Roy. Meteor. Soc.,* **133,** 595–605.

Shapiro, L. J., and H. E. Willoughby, 1982: The response of balanced hurricanes to local sources of heat and momentum. *J. Atmos. Sci.,* **39,** 378–394.

Sitkowski, M., J. P. Kossin, and C. M. Rozoff, 2011: Intensity and structure changes during hurricane eyewall replacement cycles. *Mon. Wea. Rev.,* **139,** 3829–3847.

——, ——, ——, and J. Knaff, 2012: Hurricane eyewall replacement cycle thermodynamics and the relict inner eyewall circulation. *Mon. Wea. Rev.,* in press.

Skamarock, W. C., J. B. Klemp, J. Dudhia, D. O. Gill, D. M. Barker, W. Wang, and J. G. Powers, 2005: A description of the Advanced Research WRF Version 2. NCAR Tech. Note NCAR/TN-468+ST, 88 pp.

Smith, R. K., and M. T. Montgomery, 2010: Hurricane boundary-layer theory. *Quart. J. Roy. Meteor. Soc.,* **136,** 1665–1670.

——, ——, and S. Vogl, 2008: A critique of Emanuel's hurricane model and potential intensity theory. *Quart. J. Roy. Meteor. Soc.,* **134,** 551–561.

——, ——, and N. Van Sang, 2009: Tropical cyclone spin-up revisited. *Quart. J. Roy. Meteor. Soc.,* **135,** 1321–1335.

Terwey, W. D., and M. T. Montgomery, 2008: Secondary eyewall formation in two idealized, full-physics modeled hurricanes. *J. Geophys. Res.,* **113,** D12112, doi:10.1029/2007JD008897.

Wang, Y., 2008a: Rapid filamentation zone in a numerically simulated tropical cyclone. *J. Atmos. Sci.,* **65,** 1158–1181.

——, 2008b: Structure and formation of an annular hurricane simulated in a fully compressible, nonhydrostatic model—TCM4. *J. Atmos. Sci.,* **65,** 1505–1527.

——, 2009: How do outer spiral rainbands affect tropical cyclone structure and intensity? *J. Atmos. Sci.,* **66,** 1250–1273.

Willoughby, H. E., J. A. Clos, and M. G. Shoreibah, 1982: Concentric eyewalls, secondary wind maxima, and the evolution of the hurricane vortex. *J. Atmos. Sci.,* **39,** 395–411.

Wu, C.-C., H.-J. Cheng, Y. Wang, and K.-H. Chou, 2009: A numerical investigation of the eyewall evolution of a landfalling typhoon. *Mon. Wea. Rev.,* **137,** 21–40.

——, Y.-H. Huang, and G.-Y. Lien, 2012: Concentric eyewall formation in Typhoon Sinlaku (2008). Part I: Assimilation of T-PARC data based on the ensemble Kalman filter (EnKF). *Mon. Wea. Rev.,* **140,** 506–527.

Xu, J., and Y. Wang, 2010a: Sensitivity of tropical cyclone inner core size and intensity to the radial distribution of surface entropy flux. *J. Atmos. Sci.,* **67,** 1831–1852.

——, and ——, 2010b: Sensitivity of the simulated tropical cyclone inner-core size to the initial vortex size. *Mon. Wea. Rev.,* **138,** 4135–4157.

Zhang, Q.-H., Y.-H. Kuo, and S.-J. Chen, 2005: Interaction between concentric eye-walls in super typhoon Winnie (1997). *Quart. J. Roy. Meteor. Soc.,* **131,** 3183–3204.

Zhou, X., and B. Wang, 2011: Mechanism of concentric eyewall replacement cycles and associated intensity changes. *J. Atmos. Sci.,* **68,** 972–988.